2009

AN INVESTIGATION INTO THE DESIGN AND CONSTRUCTION OF A LOW REYNOLDS NUMBER SWIMMER

Bryan Godbolt

AN INVESTIGATION INTO THE DESIGN AND CONSTRUCTION OF A LOW REYNOLDS NUMBER SWIMMER

(Spine Title: DESIGN OF A LOW REYNOLDS NUMBER SWIMMER)

(Thesis Format: Monograph)

by

Bryan Godbolt

Graduate Program in Engineering Science

Department of Electrical and Computer Engineering

A thesis submitted in partial fulfilment

of the requirements for the degree of

Master of Engineering Science

The School of Graduate and Postdoctoral Studies

The University of Western Ontario

London, Ontario, Canada

ABSTRACT

This work was motivated by the goal of building a robot capable of swimming on a microscopic scale by changing its shape. Two approaches to low Reynolds number swimming are studied. A deformable sphere is investigated which uses a method of construction called tensegrity to allow changes in shape. We found a method of matching tensegrity spheres to desired shapes and investigated the use of shape memory alloy coils as tensile elements. We propose a model for a box-shaped deformable swimmer, and a prototype is built and tested. The negative results from the prototype tests are then investigated by measuring the drag forces caused by pushing different block sizes through high viscosity fluid. Based on our experimental results we validate our approach and recommend design modifications for a second generation robot.

Keywords: low Reynolds number, biomimetic swimming, robotic amoeba

ACKNOWLEDGMENTS

Many thanks go to Dr. Rajni Patel for graciously allowing us the use of his lab space in which to conduct our experiments. Thanks to Dr. Tony Straatman for taking the time to consult with me on the use of computational fluid dynamics solvers. Thanks also to Dr. André Boivin for spending many afternoons in July and August of 2007 teaching me the fundamentals of real analysis, then against his better judgement, allowing me to enrol in his course on metric spaces.

I would also like to thank Curtis Cleaver who spent many late nights with me building model tensegrity spheres and measuring the force applied by SMA coils.

I have enjoyed my time in the Computer Vision and Mobile Robotics Lab and in particular I would like to thank Mehdi Delrobaei for his insightful advice, Duane Jacques for helping me to solder together some of the electronics, and Dave Michel for helping me to edit this document and for helping me empty a barrel of polydimethylsiloxane into my tank.

Finally, I would like to thank Dr. Ken McIsaac for supervising my research. I have learned much more than I could possibly list from our many, many conversations. I will carry his lessons and advice with me in all of my future endeavours.

Contents

List of Figures

Chapter 1

Introduction

1.1 Motivation

Underwater swimming is an area which is currently of wide interest. In this field microscopic swimming presents a particular challenge because unlike the macroscopic case conventional propulsion by propellers or jets is not possible. Indeed this environment is characterized by a very low Reynolds number, which means that viscous forces dominate the inertial forces (we give a more detailed discussion in Section 1.2.2). However, micro-swimmers could have many important applications. In particular medical uses are driving a lot of research in the field. Procedures such as endoscopy [1,2,3] or minimally invasive surgery could be greatly enhanced with the use of micro robotic swimmers. Although some advanced systems exist for endoscopy [4] or other types of sensors [5] they still move using the internal currents of the intestines. A micro-swimmer could reach places that pills cannot be carried by biological flows. Faced with the challenge of building a microscopic robot many designers look to nature for inspiration. This biomimetic approach has resulted in several projects based on flagellar propulsion. Another area of interest which is also motivated by a biomimetic approach but is much less studied is swimming by self deformation. This is the area into which we chose to conduct our research.

1.2 Background on Biomimetic Swimming

There are two main classes of biomimetic swimming approaches at high Reynolds number. Anguilliform swimming uses a wave that has nearly constant amplitude across the entire body and neglects the effect of vortex shedding in the wake. Carangiform locomotion, by contrast, uses a wave that has much larger amplitude in the tail and relies on the effect of vortices for propulsion. In addition there are biomimetic swimming strokes that do not use a body wave for propulsion, but rely on flapping fins.

Anguilliform locomotion receives its name because it is the type of swimming used by an eel. McIsaac and Ostrowski [6] present their results from experiments with a 5 link eel-like swimming robot (REEL II). Their experimental setup was used by Cortes et al. [7] who present optimal gaits for this eel although the results apply to more general systems. In more recent work an eel-like robot which uses a continuous model and is capable of three dimensional motion was built by Khalil et al. [8].

There are also several examples of robots using carangiform style propulsion. Trout, tuna and dolphins are examples of animals which use this style of locomotion which is extremely efficient and can lead to very high speed swimming. Triantafyllou and Triantafyllou report their results from a robot tuna they built in [9]. Similarly a robotic pike was built by Kumph [10]. Following these results Anderson and Chhabra [11] built a mission scale underwater vehicle which could swim like a yellowfin tuna called VCUUV. Nakashima and Ono describe their robotic dolphin in [12]. They followed this work with a dolphin capable of three dimensional motion [13]. In particular they were able to stabilize and analyze the loop-the-loop motion. Liu et al. present a design for a fish robot capable of three dimensional swimming which uses only one motor in [14]. Mason and Burdick model carangiform propulsion and then confirm it experimentally with a three link robot in [15]. Yamamoto and Terada [16] built a robotic fish at Mitsubishi which was intended for aquariums at an amusement

park but also showed applications to underwater vehicles. Yu et al. present their experimental results of a 4 link robot fish with a hybrid controller in [17]. Then in [18] they present a multi-link fish capable of 3-D motion.

There have also been robotic fish reported which do not fit into either of these categories, but use fin motion to swim. Ayers et al. [19] built an underwater vehicle based on a sea lamprey using shape memory alloy artificial muscles. Kato [20] presents a robotic bass which swims with two pectoral fins and is capable of lateral motion and docking with an underwater post even in water currents. Low and Willy [21] designed a modular ribbon style fin which they built and attached to a robotic knifefish.

Various methods of actuation for use in fish-like robots have also been reported. Guo et al. built and tested a fish-like robot using ionic conducting polymer film actuator for propulsion in [22]. Propulsion from an SMA actuator is reported by Fukuda et al. in [23]. Fukuda et al. present a method of swimming using PZT actuator in [24]. They present a method for steering such a robot in [25].

1.2.1 Background on Micro-Swimmers

Much of the current research into developing a microscopic swimming robot uses a biomimetic approach. Indeed microorganisms have had millions of years to evolve their mechanisms for propulsion, thus it follows that looking to nature for inspiration is a logical approach. In particular many designs which employ a flagellar approach to locomotion have been studied. Kosa et al. [1] designed a swimming endoscope which using two flagella which would be able to swim in water. They followed this work with another design which is powered by the static magnetic field of an MRI [2,3]. Behkam and Sitti analyze two types of flagellar propulsion as well as measure the thrust force of a helical wave experimentally in [26]. Yu et al. built a robot with a flagellar type propulsion system and measured the force it generated in a low Reynolds number environment using a strain gauge in [27]. Edd et al. present a design for a micro

robot using a helical motor using nano tubes in [28]. Analysis of the fluid dynamics of this type of propulsion has also been performed. Brennen and Winet give a detailed overview in [29]. Wiggins and Goldstein [30] present a detailed analysis of a swimmer which uses flexible elastic elements. Hancock obtains formulae for the velocity and propulsion of an infinite filament with travelling waves in [31].

A similar type of motion which was originally proposed by Purcell [32] is a swimmer made of straight connected links. The angle between the links can be controlled. This configuration, which requires a minimum of three links, has been analyzed by Becker et al. [33]. They also demonstrate the importance of anisotropic motion at low Reynolds number, which is the idea that a two link swimmer can only have a time reversible stroke and therefore cannot swim. Using a similar idea Zhang and Liu [34] analyze, simulate and build a bidirectional swimming robot driven by a magnetic field. Their prototype robot was able to swim through a pipe.

Biomimetic locomotion is not the only type of propulsion which has been studied. Indeed, there are many approaches to low Reynolds number swimming which are not inspired by nature, and may even be more appropriate for micro-robots. Yesin et al. built a magnetic micro-robot and were able to measure drag forces experimentally as well as steer it through a maze in [35]. Ishiyama et al. present their experimental results from a screw like micro-machine driven by a magnetic field in [36, 37]. They also performed finite-element analysis on their design which is reported in [38]. Finally, they describe a method for trailing a wire behind their swimmer in [39]. They conclude that their robot has potential for procedures such as inserting a catheter. Other work which deals directly with the problem of miniaturization of propulsion methods was done by Dreyfus et al., who show that a linear chain of colloidal magnetic particles linked by DNA and attached to a red blood cell can act as a flexible artificial flagellum in [40]. Another example is Kulic et al. [41] who describe a method for building a nanomotor out of twirling DNA rings.

Results from purely analytical methods have been found for both biomimetic and non-biomimetic shapes. Lighthill [42] introduces the idea of a deformable sphere which can swim at low Reynolds number. Blake [43] uses a similar idea for deformable infinite cylinders. Kelly and Murray also analyze the motion of deforming infinite cylinders in [44]. However, their work focuses a geometric approach to the control of locomotion. A prototype robot based on this idea was built by Chen [45]. Higdon describes the dynamics of a spherical swimmer with a cylindrical tail which uses helical waves to move in [46]. Avron et al. develop a method of swimming by moving fluid between bladders in [47]. Similarly, Leshansky et al. present a method of low Reynolds number propulsion by way of surface treadmilling in [48]. This design employs a thin rod which can have a large bulge that starts at one end and moves to the other. Leshansky and Kenneth [49] also present a method of swimming by rotating rings of spheres. This work uses the results of Filippov [50] who generalized Lamb's results [51] for the drag caused by a sphere at low Reynolds number, to the case of N non-overlapping spheres. Leshansky presents a model for actin-based propulsion of a micro-swimmer in [52]. This process uses the polymerization growth of a tail to push an object forward. Another design originally suggested by Purcell [32] is that of three spheres connected in a line such that the distance between them can be varied. Najafi and Golestanian analyze the fluid dynamics of this design in [53] and predict its motion. Alouges et al. frame the problem in terms of control theory and are able to prove controllability for the design and thus confirm it can swim in [54]. They also present a method to compute optimal strokes.

Efficiency is also studied extensively for micro-swimmers. Since a power source would be difficult to design to fit on a microscopic robot, it is important to design propulsion to use the available energy as efficiently as possible. Lighthill introduces the idea of efficiency in [42] as the ratio of mean power exerted by a body to the power required by the fluid to resist its motion. Tam and Hosoi present a three link swimmer

design which is optimized for efficiency in [55]. Avron et al. introduce the notion of a swimming drag coefficient which allows swimmers to be ranked based on efficiency in [56]. These values are compared to the work of Chattopadhyay et al. who measured the force and power generated by E. coli bacteria and thus measure the efficiency of their swimming in [57]. For a more general case Shapere and Wilczek [58,59] analyze the geometry of swimming at low Reynolds number and discuss the efficiency. Stone and Samuel also analyze the efficiency of deformations and derive an upper bound on their efficiency in [60]. In these works, deformation is used in the general sense and refers to arbitrary shape change by body reconfiguration.

1.2.2 Low Reynolds Number Fluid Dynamics

The **Reynolds number** is the ratio of intertial forces to viscous forces in a fluid. It is used to characterize the fluid dynamical regime of an environment. The ratio is defined in Equation (1.1) where u is velocity, L is the characteristic length, and ν is the kinematic viscosity [61].

$$Re = \frac{uL}{\nu} \tag{1.1}$$

There are some important consequences of a very low Reynolds number. In particular, drastic simplifications can be made to the Navier-Stokes equations, and swimming strokes cannot be time reversible (Section 1.2.3).

The Navier-Stokes equations are used to model fluid flow. By making the assumption of an incompressible Newtonian fluid and invoking a coordinate system in a Euclidean space the Navier-Stokes equations are defined as,

$$\rho\left(\frac{\partial \boldsymbol{v}}{\partial t} + (\boldsymbol{v}\cdot\boldsymbol{\nabla})\boldsymbol{v}\right) = -\nabla p + \mu\nabla^2\boldsymbol{v} + \mathbf{f} \tag{1.2}$$

$$\boldsymbol{\nabla}\cdot\boldsymbol{v} = 0 \tag{1.3}$$

where ρ is the density, $\boldsymbol{v}$ is the velocity, p is the pressure, μ is the viscosity, and $\mathbf{f}$ are the externally applied forces.

Stokes flow, which we will also refer to as **creeping flow**, refers to the fluid dynamical regime which occurs when the Reynolds number goes to zero, $Re \rightarrow 0$. The assumption of Stokes flow [62] reduces the Navier-Stokes equations in the presence of no external forces to Equations (1.4) and (1.5) which are known as the Stokes equations.

$$\nabla p = \mu \nabla^2 \boldsymbol{v} \tag{1.4}$$

$$\nabla \cdot \boldsymbol{v} = 0 \tag{1.5}$$

The Stokes equations do not take the inertial terms into account, which means they become linear. However, even with this linear model analytical solutions are often not possible in the presence of certain boundary conditions.

1.2.3 The Scallop Theorem

The **Scallop Theorem** [32], which is also known as the **Reciprocal Theorem** [63], states that the net displacement of a body using a cyclic gait may only occur by a non time reversible sequence of body shape changes. This is to say, time is not a factor in a low Reynolds number environment, only the internal configuration of a body determines its position in space. In other words the speed at which a body deforms does not affect how far the body will move, only the amount of time required to travel the distance. Consequently a body with only one degree of freedom cannot move at low Reynolds number. Purcell [32] refers to this phenomenon as the Scallop Theorem since the swimming stroke of a scallop forms an illustrative example which we have depicted in Figure 1.1. At high Reynolds number the scallop swims by closing its

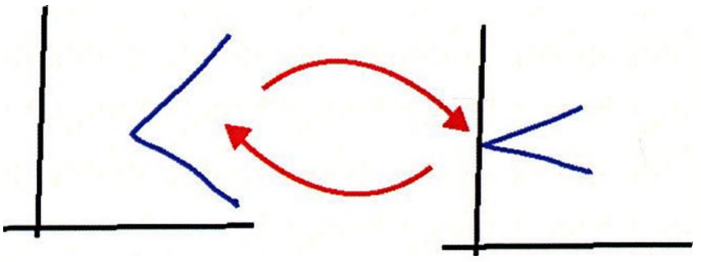

Figure 1.1: The Scallop Theorem

shell rapidly and ejecting a jet of water which causes it to glide forward, then opening its shell slowly so that it doesn't move backwards as far. This stroke will not result in net displacement at low Reynolds number because the speed that the shell closes will not affect how far the scallop moves.

This theorem is essential to our discussion of swimming because intuitive swimming strokes based on our interactions with the physical world are invalid at very low Reynolds number. Another illustrative example might be a canoeist who propels herself without removing her paddle from the water. Although inefficient, this is possible in a fluid with non-negligible inertia such as water because the drag caused by the paddle varies nonlinearly with the speed that the paddle moves, and because impulses caused by paddle strokes can cause significant drift. In this way her canoe can have net displacement in the forward direction by moving the paddle quickly in the first half of the stroke and slowly as it returns in the second half.

1.2.4 Swimming Cylinders

Previously, shape sequences have been proposed which are designed to swim at low Reynolds number. They are based on infinitely long cylinders with low amplitude oscillatory surface deformations [44, 58, 42, 43]. The use of an infinite cylinder allows edge effects to be discarded, and thus the problem need only be considered in a plane whose normal is parallel to the axis of the cylinder. Even though the assumption of creeping flow reduces the Navier-Stokes equation to a linear partial differential

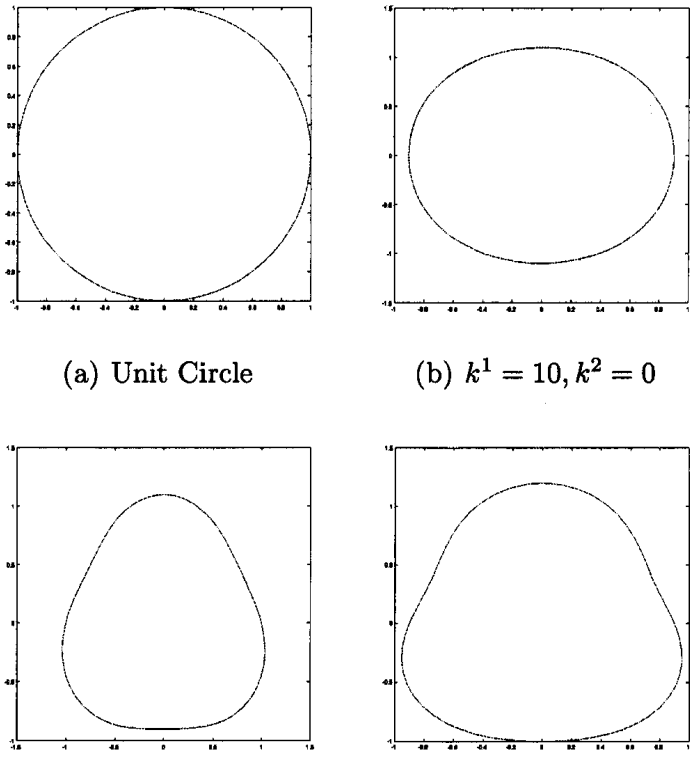

(a) Unit Circle (b) $k^1 = 10, k^2 = 0$

(c) $k^1 = 0, k^2 = 10$ (d) $k^1 = 10, k^2 = 10$

Figure 1.2: Swimming stroke based on Equation (1.6)

equation, it is only possible to solve for certain boundary conditions using classical methods. Thus, there is strong motivation in analytical work for continuous shapes to be used. We based our work largely on the following example which was originally proposed by Kelly and Murray [44]. The radius of the cylinder, r is given by,

$$r(t, \theta) = 1 + \epsilon(k^1(t)cos(2\theta) + k^2(t)cos(3\theta)), \tag{1.6}$$

where ϵ is a small parameter, and k^1, k^2 are shape control parameters. They show that the cylinder's motion will be of the form,

$$\dot{x} = -\epsilon^2 \left(\frac{k^2 \dot{k}^1}{4} + \frac{k^1 \dot{k}^2}{2} \right) + O(\epsilon^3). \tag{1.7}$$

However these results have never been tested in practice. In one case a pro-

totype robot was constructed which was capable of deforming into shapes similar to the ones in this section [45]. However, this robot was tested in water which does not maintain the appropriate Reynolds number necessary to determine its ability to swim. Additionally it was based on a design where water was required to be pumped into and out of the robot from an external source. It is difficult to imagine that such a robot could be self propelled.

1.3 Research Goals

The main goal of this research was to investigate a method of low Reynolds number swimming which used a changing sequence of body shapes for locomotion. Our intention was to use this robot as an experimental platform for investigations into a class of geometric control problems. Although we fell short of our intended goal, we were able to make significant progress towards ultimately building this type of swimmer.

1.4 Contributions

- We developed a method of matching a tensegrity structure to a deforming sphere.
- We built an experimental setup which can be used for macro-scale experiments at very low Reynolds number.
- We developed a model for the swimming stroke of a box-shaped robot and built a prototype based on the model to test it experimentally.
- We designed and built an apparatus for measuring the drag force on and object being pushed through a fluid. We were able to use this to confirm experimentally that, at a minimum there is a range of block sizes from 2-4 inches where the drag force is strictly monotonic in the characteristic length.

1.5 Organization

In Chapter 2 we describe our attempt to build a deformable sphere capable of swimming. We develop a method of matching a tensegrity structure to a sequence of shapes. In addition we show that shape memory alloy coils are suitable as actuators for this type of robot. Chapter 3 documents the design and construction of our box-shaped prototype swimmer. Finally in Chapter 4 we experimentally investigate the cause of some of the negative results from Chapter 3 suggest design modifications towards a next generation swimmer that should be capable of swimming.

Chapter 2

Design of Self-Deforming Spheres

In this chapter we describe our attempt to design a spherical swimmer. We chose a method of construction called tensegrity, which required us to formulate and solve an optimization problem to match devised shapes. We chose shape memory alloy coils for actuators and developed a method to control them.

2.1 Hypothesis

Our hypothesis was that by revolving the shape described by Kelly and Murray [44] (Figure 1.2) in an axially symmetric fashion instead of extending it into an infinite cylinder as they proposed, the shape sequences discussed in their work would still result in motion. We chose this approach because this design is finite in size and it is therefore possible to construct. However, because the shape is described by transcendental functions, it is smooth (C^∞), which makes it impossible to build exactly, using traditional methods of actuation, which are not suitable for achieving arbitrarily complex smooth shapes. The method of tensegrity provides one possible way to implement such a robot by approximating smooth shapes with a discrete set of nodes.

2.2 Tensegrity

Tensegrity is a method of construction which uses only compressive and tensile elements in a stable equilibrium to present objects that can have very complex geome-

tries. We will refer to the compressive elements as rods, and the tensile elements as strings. By changing the tension in the strings, the configuration of a structure can be modified. The idea of tensegrity along with its name was first developed by Fuller in 1959 [64]. It was originally intended for the construction of very large buildings. Tensegrity is an appealing construction technique because the structure is self supporting. Additionally, it could be used for temporary structures such as bridges or towers which could be erected rapidly. The first tensegrity structure was constructed by Snelson [65]. The dynamics of tensegrity structures have been studied extensively by Skelton [66,67,68]. Design and control of shape changing tensegrity structures has been studied by Masic [69]. Pinaud et al. developed a method of path planning for shape control of such structures in [70]. Moored and Bart-Smith show how to use optimization to approximate shapes with tensegrity in [71], focusing on a morphing wing.

We proposed to use this background to build a deformable sphere of axial symmetry as in Figure 1.2, capable of swimming at low Reynolds number. Once we had a tensegrity sphere capable of shape control, our plan was to embed the structure into a smooth, compliant skin that would complete the approximation.

2.3 Tensegrity Spheres

Tensegrity spheres are relatively easy to construct. The accuracy with which they approximate the shape of a sphere is determined by the number of elements used. Figure 2.1 shows models with 6 rods and 12 rods. The figures show how increasing the number of elements improves the approximation of a sphere. Unfortunately the design of the structure becomes very complicated. As the number of rods increases, the number of strings increases by a factor of 4. Furthermore, the structure has no structural integrity until it is complete. Indeed, during construction the model spheres we built attempted to destroy themselves right up until the last elastic was

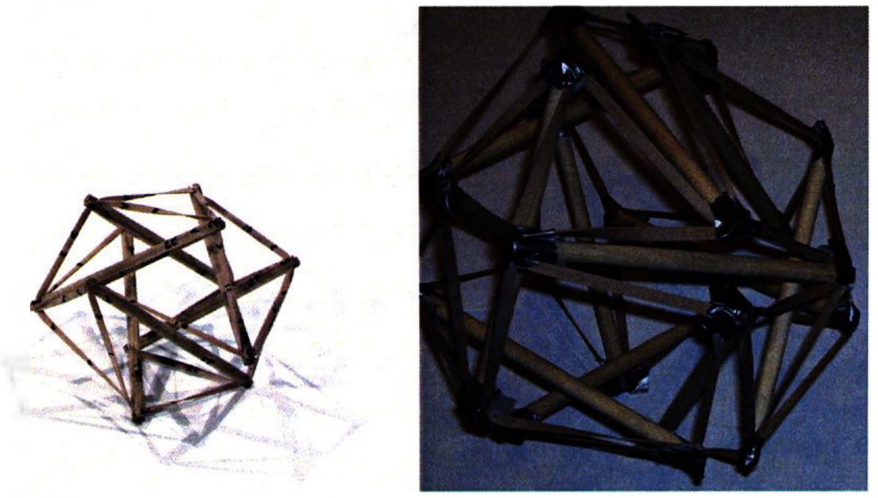

(a) 6 Strut Tensegrity Sphere (b) 12 Strut Tensegrity Sphere

Figure 2.1: Examples of two tensegrity spheres

attached. Therefore, we chose to use the 6-strut model in order to simplify construction. However, before we could proceed with construction we needed a way of determining the amount of tension required in the appropriate elements to achieve a particular perturbation of the shape.

The first step in the process was to formalize a mathematical model of the tensegrity sphere. Then we could use this result to formulate an optimization problem to match a tensegrity structure to a desired shape. The combination of string lengths and tensions of a perturbed tensegrity sphere would then provide sufficient input to control variable length actuators in a physical model.

2.4 Mathematical Description

In order to work with our tensegrity structure we required a way to model it. The reason for this was that once we had a tensegrity structure, we needed a way to match its shape to a desired shape. This section will illustrate how we represent a tensegrity structure mathematically, and the following section will discuss a method of approximating a desired shape.

This is a presentation of a combination of methods from [8] and [9]. To clarify the discussion of this topic, we will present the example of the 6 strut tensegrity sphere after we present the method. We represent the number of nodes, number of tensile elements (strings) and total number of elements as n_n, n_s, n_{el} respectively. Based on this notation, we form two matrices to represent the connectivity of the rods and the strings separately as defined in Equation (2.1). To do this, each element is given a number and a direction. This information is chosen arbitrarily, however care must be taken to maintain its consistency.

$$S \in \mathbb{R}^{n_n \times n_s}, B \in \mathbb{R}^{n_n \times (n_{el} - n_s)} \tag{2.1}$$

Matrix S represents the manner in which the nodes are connected by strings. Each column corresponds to a string and each row corresponds to a node. The majority of positions in the matrix are occupied by zeros which is to say that the matrix is sparse. However in each row (node) there are four entries of either -1 or 1 because four strings connect to each node. The -1 shows that the string emanates from the corresponding node, whereas the 1 shows that the string terminates there. Matrix B is defined in a similar way, except it represents the connectivity of the rods.

We now build a directed graph describing all the members and their direction. This is formed by a member-node incidence matrix,

$$M \in \mathbb{R}^{n_n \times n_{el}}. \tag{2.2}$$

Matrix M is also a sparse matrix which consists of matrix S augmented by B as shown in Equation (2.3).

$$M = \begin{bmatrix} -S & B \end{bmatrix} \tag{2.3}$$

We define the matrix which will actually be used in computation in (2.4).

Matrix $C \in \mathbb{R}^{3n_n \times 3n_{el}}$ is a sparse block diagonal matrix in which the block elements are copies of matrix M. The reason for this is that the three dimensions of a standard Euclidean space will correspond respectively to the rows of C.

$$C = blockdiag(M) = \begin{bmatrix} M & 0 & 0 \\ 0 & M & 0 \\ 0 & 0 & M \end{bmatrix} \tag{2.4}$$

Next, we define a vector $\lambda \in \mathbb{R}^{n_{el} \times 1}$ to represent the force densities of all the elements. Each element of λ is given by Equation 2.5.

$$\lambda_i = \frac{f}{L} = EA\left(\frac{1}{L_0} - \frac{1}{L_i}\right) \tag{2.5}$$

Equation (2.5) describes the elements of λ where E is the Young's modulus, A is the cross sectional area, L_0 is the initial or manufacturing length of a member and L_i is the final length. For the strings maximum and minimum lengths are specified, whereas the rods are considered to be constant length. These lengths are nonlinear functions of a node vector

$$p = \begin{bmatrix} x \\ y \\ z \end{bmatrix}, p \in \mathbb{R}^{3n_n \times 1} \tag{2.6}$$

whose elements are the three Cartesian coordinates of the nodes in the following form

$$L_i = \sqrt{(p_{sx} - p_{fx})^2 + (p_{sy} - p_{fy})^2 + (p_{sz} - p_{fz})^2} \tag{2.7}$$

where p_{sx}, and p_{fx} are the x ordinates of the emanating and terminating nodes for member i.

We define $\hat{\lambda} \in \mathbb{R}^{3n_{el} \times 3n_{el}}$ to be the diagonal form of λ.

$$\hat{\lambda} = blockdiag(diag(\lambda)) = \begin{bmatrix} \lambda_1 & 0 & 0 & 0 & 0 & 0 \\ 0 & \lambda_2 & 0 & 0 & 0 & 0 \\ 0 & 0 & \ddots & \vdots & \vdots & \vdots \\ 0 & 0 & \cdots & \lambda_{n_{el}} & 0 & 0 \\ 0 & 0 & \cdots & 0 & \lambda_1 & 0 \\ 0 & 0 & \cdots & 0 & 0 & \ddots \end{bmatrix} \tag{2.8}$$

Finally, using the method of virtual work [71] we can find the force required for a particular configuration by

$$C\hat{\lambda}(p)C^T p = f_{ext}, \ \|\hat{\lambda}(p)\| > 0, f_{ext} \in \mathbb{R}^{3n_n \times 1} \tag{2.9}$$

where f_{ext} is the externally applied force in each element in order to achieve the node position described by p. Therefore we can say that the equilibrium configuration of the tensegrity structure is defined by,

$$C\hat{\lambda}(p)C^T p = 0, \ \|\hat{\lambda}(p)\| > 0 \tag{2.10}$$

which is the case where the externally applied forces are all 0.

Using this representation the tensegrity structure can easily be programmed into Matlab. It should be noted that the length of the members can be calculated by

$$L = C^T p$$

2.4.1 Example: Six Strut Tensegrity Sphere

For this case we begin by labelling all the elements with a number and a direction. Node and element numbers are chosen arbitrarily and our choices are shown in Fig-

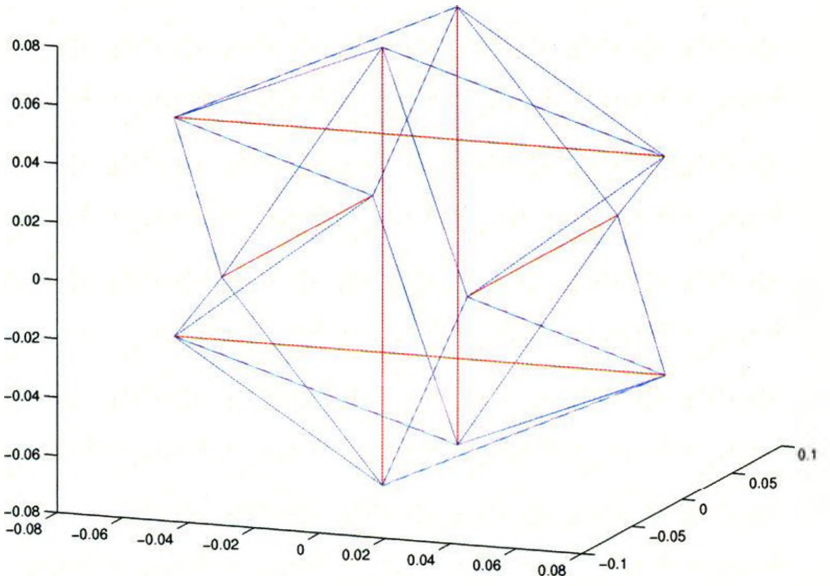

Figure 2.2: Matlab plot of tensegrity sphere using connectivity matrix

ure 2.1(a). The first few entries in our S matrix is shown in (2.11)

$$\begin{bmatrix} 0 & 0 & 0 & -1 & \cdots \\ 0 & -1 & -1 & 0 & \cdots \\ -1 & 0 & 1 & 1 & \cdots \\ \vdots & \vdots & \vdots & \vdots & \ddots \end{bmatrix} \tag{2.11}$$

Our B matrix is formed in a similar way. With these matrices defined, and given a node position matrix p, we can use Matlab to plot the tensegrity structure. An example is shown in Figure 2.2.

2.5 Shape Approximation

Using the description of a tensegrity structure defined in the previous section we must now consider a method of approximating this structure to the shape sequence defined

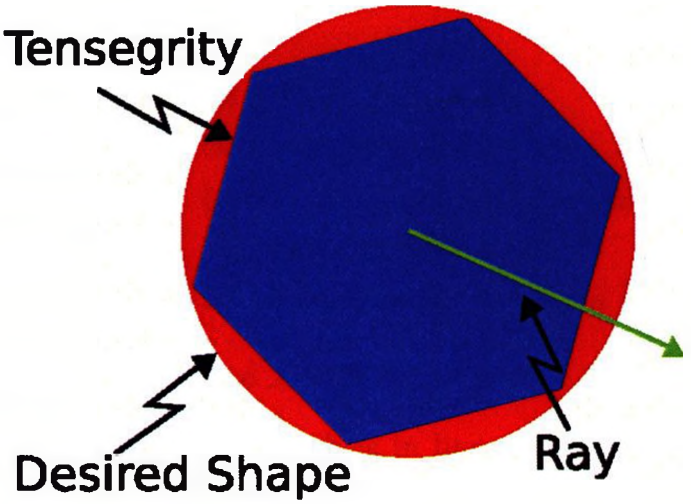

Figure 2.3: Objective Function

by Equation 1.6. To accomplish this our plan was to first discretize the shape sequence in time, then find a mapping to perturb the tensegrity sphere to each discretized shape. The initial condition for each time step would be the configuration in the previous time step. This approach allows for the calculations required to perform the shape matching to be done offline. Finally, interpolating between the discrete shapes would be used to reconstruct an approximation of the continuous shape sequence. The overall method used for shape approximation was to minimize the error between the tensegrity structure and the desired shape. We formulated this error as an objective function which was then used to search for an optimal configuration.

For an objective function we considered the centroid of the structure to be the origin. We then considered a ray from the origin through a node on the structure and found its point of intersection with the continuous desired shape (Figure 2.3). The absolute value of the distance between this point and the corresponding node was then calculated for each node and added together to form the error between the shapes. The absolute value was used so that there would be no negative errors causing unwanted cancellation. The objective function we used was formally defined as follows.

$$\text{Let } \begin{cases} M = \mathbb{R}^3, & \text{be a Euclidean space} \\ d : M \times M \to [0, \infty), & \text{be the canonical metric on } M \\ S, & \text{be the set of all two dimensional} \\ & \quad \text{surfaces embedded in } M \\ \mathbb{X}, & \text{be all possible finite sets in } M \text{ with } n_n \text{ elements} \end{cases}$$

Choose some $S_0 \in S$. Then for some $X \in \mathbb{X}$ we take each $x_i \in X : i \in \{1...n_n\}$ and define $y_i \in S_0$ to be the point on S_0 which is in line with x_i and the centroid of S_0. Our objective function is then defined as

$$f : \mathbb{X} \times S \to [0, \infty), \text{ such that} \tag{2.12}$$

$$f(X, S_0) = \sum_{0 \leq i < n_n} d(x_i, y_i), \forall X \in \mathbb{X} \tag{2.13}$$

we then find the optimal configuration $\hat{X} \in \mathbb{X}$ such that

$$|f(\hat{X}, S_0) - \inf_{X \in \mathbb{X}} f(X, S_0)| < \epsilon \tag{2.14}$$

for some acceptable tolerance $\epsilon \in (0, \infty)$, and where $\inf U$ denotes the greatest lower bound on U for some $U \subset \mathbb{R}$. We perform this optimization subject to the constraints that the distance between nodes connected by rods is fixed and the distance between nodes connected by strings has extrema stemming from the physical implementation. In our case of shape memory alloy coils the minimum length was 5 cm and a maximum length of 14 cm.

To implement our optimization problem we used a function in the Matlab Genetic Algorithm and Direct Search Toolbox called patternsearch to perform the optimization. Patternsearch minimizes an objective function, subject to user defined constraints, to solve nonlinear optimization problems. In this case the constraints

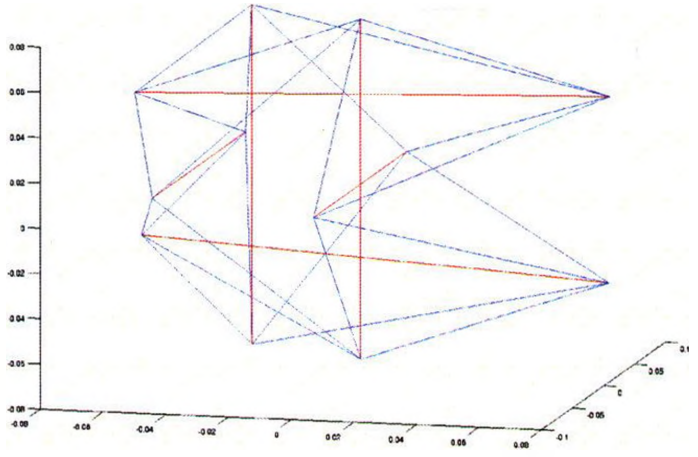

Figure 2.4: Resulting tensegrity

were the physical lengths of the elements. This computation left us with a node position vector p which defined the new shape of the tensegrity structure. In order to calculate the forces required to take on this configuration we used the method described by Equation (2.9).

2.6 Results

We found that although our overall procedure succeeded, the shape approximations did not adequately match the desired shapes. Figure 2.4 shows the result of attempting to match the shape obtained by revolving Figure 1.2(d). Although one can imagine how this shape in some way corresponds to the desired shape, it is clear that it does not constitute a sufficiently accurate approximation. To smoothly approximate desired shapes many more than six struts would be required. The increasing complexity of the structures meant this was not a feasible approach to designing and building a robot for exploring the low Reynolds number swimming problem.

2.7 Actuators for Tensile Elements

We knew from the outset of our work on tensegrity that we required a low-weight, low cost actuator to act as the tensile elements. Shape memory alloy (SMA) coils were a natural choice. Thus, concurrently with our work on tensegrity, we developed an experiment to help us design the control of the coils.

In order to use the actuators we needed to develop a way of controlling the force. The easiest way of doing this would be to use open loop control. However we needed to know if this was possible. In the case that open loop control of the coils was unreliable, we would need to have a position sensor attached to each coil in order to form a feedback loop in our controller design. The drastic difference in design complexity that this would cause led us to investigate the relationship between current and force in an SMA coil.

2.7.1 Background

The shape memory effect was first discovered in Au-Cd by Chang and Read in 1951 [72]. Following this work, the shape memory effect was found in several different alloys [73, 74]. However it was not until the work of Wang and Buehler [75, 76, 77] who discovered the effect in Ni-Ti, that it was able to be used as an actuator. They developed Ni-Ti wire or Nitinol. When the wire is cool it can be deformed easily, however when it is heated above a threshold it will return to its original shape. When this wire is formed into a coil it is able to vary its length by a large percentage. Additionally it can be made to either expand or contract. Its electrical properties make it convenient as an actuator because its temperature can be controlled by the current passing through it.

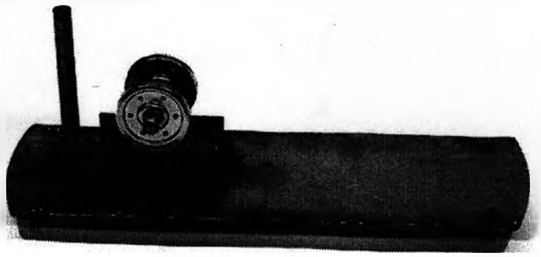

Figure 2.5: Experimental Apparatus for Force-Current Experiment

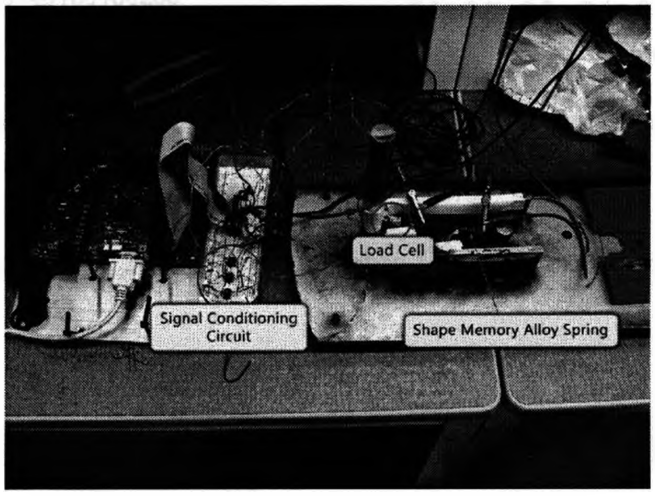

Figure 2.6: Experimental Setup for Force-Current Investigation

2.7.2 Experimental Apparatus

We designed an experiment to determine the relationship between force and current. Figure 2.5 shows the apparatus we constructed. It consisted of two fixed posts to connect an SMA coil and load cell for force experiments, as well as a track and cart to conduct position control experiments. Figure 2.6 shows the experimental setup we used. For this experiment we used a Motorola HCS12 board for data collection in addition to some operational amplifiers for signal conditioning. We also needed high current N-type mosfet transistors to control the current in the coil.

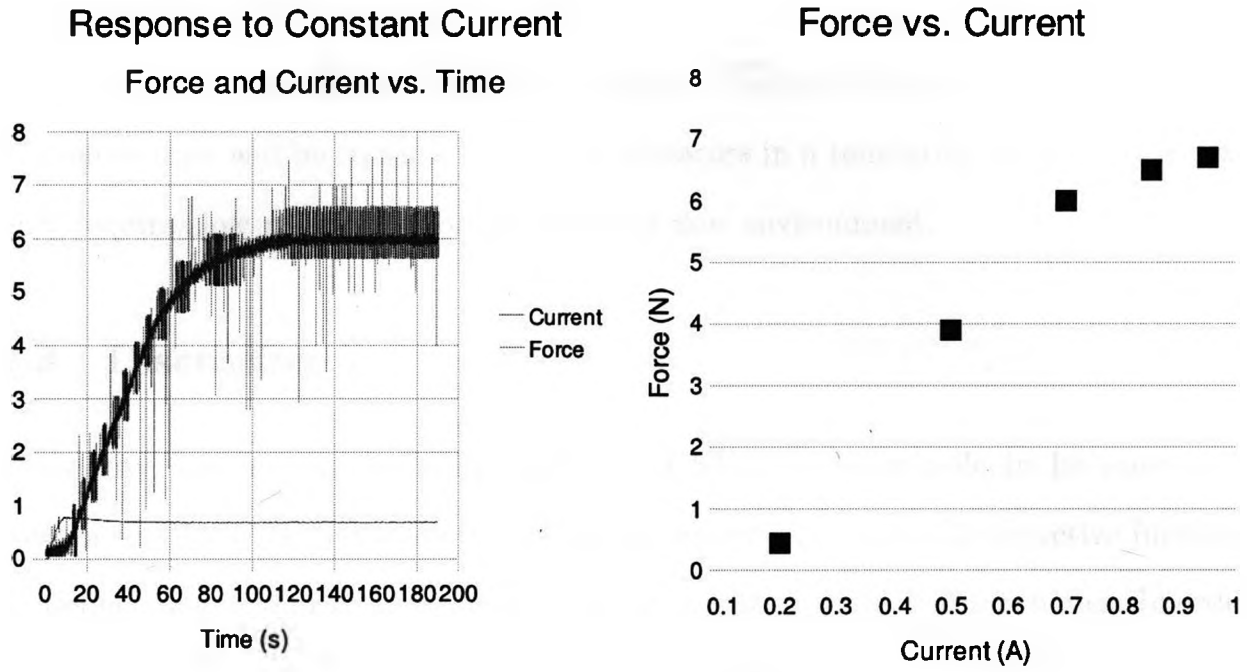

(a) Typical response to constant current

(b) Steady state force response for different currents

Figure 2.7: Results from Force-Current experiment

2.7.3 Method

The load cell was connected in series to an SMA coil. Current was applied through the SMA coil and the force it exerted on the load cell was measured. Tests were run with both a step input current as well as a pulse.

2.7.4 Results

Plots of the results from this experiment are shown in Figure 2.7. Figure 2.7(a) shows the typical response of an SMA coil to constant current. The force clearly reaches a steady state after a brief transient period. Figure 2.7(b) shows force plotted against current for five different trials. This plot is consistent with the expected SMA response for increasing current, and shows that the force will be predictable as a function of current and is therefore appropriate for open loop control.

2.7.5 Conclusion

We can control the force in the SMA coils by simply performing current control. Therefore they will be suitable for use as actuators in a tensegrity sphere because we only require slow movement for our creeping flow environment.

2.8 Discussion

Tensegrity spheres can be built readily and SMA coils are able to be open loop controlled. However, our a 6-strut tensegrity sphere subject to the objective function we defined does not provide an adequate approximation of the desired shapes. In order to achieve a sufficient level of accuracy in our approximation two things are probably necessary. First, we would need to start with a tensegrity sphere with significantly more elements. Second, a more sophisticated objective function would need to be used for the shape matching optimization problem. For example we considered another objective function which involved calculating the volume of the tensegrity structure and finding the difference between it and the volume of the continuous shape. However we did not implement it initially because calculating the volume of the discontinuous tensegrity structure would be significantly more difficult than using the first method, which we thought would be a reasonable initial attempt.

Since the purpose of this work was to investigate low Reynolds number swimming, not methods of tensegrity structure construction, we felt that it was prudent to attempt a different approach to solving this problem.

Chapter 3

Design and Construction of a Prototype Swimmer

In this section we describe our attempt to build a robot capable of swimming at low Reynolds number. Based on theoretical results we design a swimming stroke that should lead to net motion under the assumption of creeping flow.

3.1 Background

Based on the work of Brenner [63] we have two important results. First, the reciprocal theorem implies that force is proportional to velocity. Indeed we know in general that drag force F will be some function of velocity,

$$F = f(v), \tag{3.1}$$

but given the fact at that at low Reynolds number distance travelled does not depend on speed, it can be shown that force has the form shown in Equation (3.2) in which the force depends only on a parameter $k(s)$, which is defined by the shape, and the velocity. We consider s to be some parameter which defines the shape. The negative sign is included so that $k(s)$ is positive.

$$F = -k(s)v \tag{3.2}$$

We make the assertion that $k(s)$ is strictly monotonic in s, where s is the

characteristic length.

$$\text{Let } k : [0, \infty) \rightarrow [0, \infty)$$
$$\forall s_1, s_2 \in [0, \infty) : s_2 > s_1$$
$$\text{then } k(s_2) > k(s_1)$$

We do not have explicit theoretical results to support this claim for rectangular prisms, however this property has been shown for other shapes. Lamb [51] shows the following three cases. For a sphere he shows the drag resistance to be

$$F = -6\pi\mu a U \tag{3.3}$$

where, U is the velocity, and a is the radius of the sphere. Equations 3.4 and 3.5 represent the drag force required to move an infinitesimally thin disk of radius a at speed U broadside and edgeways, respectively.

$$F = -16\mu a U \tag{3.4}$$
$$F = -\frac{32\mu a U}{3} \tag{3.5}$$

In all cases the drag is strictly monotonic in radius, which for circular objects is the characteristic length.

The second important result given by Brenner [63] is that "every arbitrary particle must possess at least three mutually perpendicular axes, fixed in it, such that if it be moving parallel to one of them it will experience a force only in this direction; that is, there will be no lateral forces." This result allows for a drastic simplification in our model because we can decouple forces acting along axes, providing we only apply

forces in one direction at a time. Based on these results we are able to construct a model for our swimming stroke.

3.2 Experiment Overview

Our primary goal was to develop a design for a robot that could swim at low Reynolds number and which would be simple to build. The concept for the robot was a cube that could swim in two dimensions by extending and retracting its sides (we will use the term wing to refer to the moving sides). We designed the robot with four degrees of freedom, but we mapped out an initial swimming stroke which only used two. The swimming stroke is shown in Figure 3.1 and shows one complete cycle.

For the purpose of analysis we divided the stroke into four phases, as shown in Figure 3.1. The free body diagrams for the first phase are shown in Figure 3.2. The figure shows three free body diagrams which represent the three interactions taking place during the first phase of the stroke are shown in Figure 3.1(a), where F_r is the reaction force when the motor applies force F_a to the wing, and F_{d_a} and F_{d_r} are the drag forces due to F_a and F_r respectively. The free body diagrams for the third phase differ only in that all forces act in the opposite direction. We observe from these diagrams that since the forces are always balanced, the magnitudes of all forces are equal.

Based on Equation (3.2) we must define our dependence on shape. For the purpose of this investigation we make an approximation, and consider the shape parameter for the wing, k_w to be constant. We then pick the extrema of the shape parameter for the bulk,

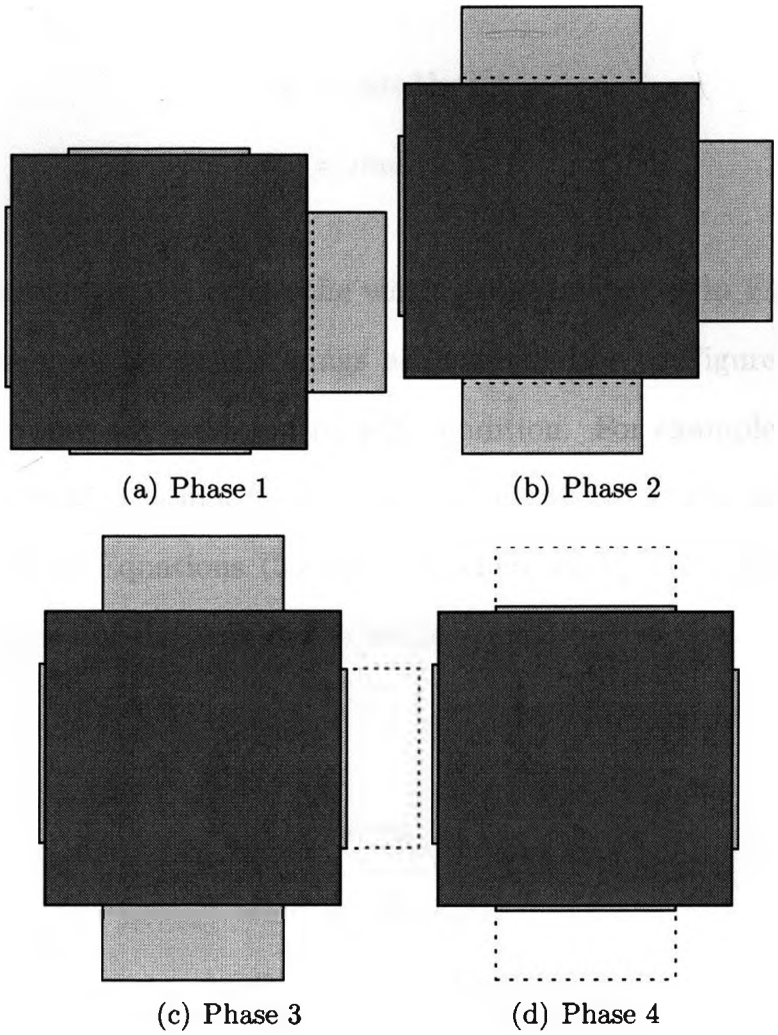

Figure 3.1: Complete swimming stroke

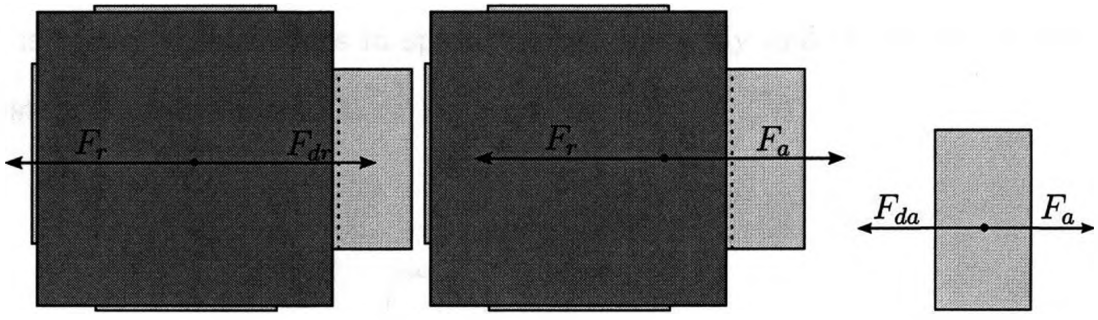

Figure 3.2: Free body diagrams showing forces during phase 1

$$k_{b_1} = min(k_b(s)) \tag{3.6}$$

$$k_{b_2} = max(k_b(s)) \tag{3.7}$$

where k_{b_1} represents the case where the wings are retracted as in Figure 3.1(d), and k_{b_2} represents the case where the wings are extended as in Figure 3.1(b). At the boundary of the robot we assume a no slip condition. For example the interface of the wing and the fluid, the fluid is assumed to be moving at the same speed as the wing. This results in Equations (3.8)-(3.10), where $v_w(t)$ is the speed of the wing, and $v_b(t)$ is the speed of the bulk of the body.

$$F_a(t) = -F_r(t) \tag{3.8}$$

$$F_a(t) = -k_w v_w(t) \tag{3.9}$$

$$F_r(t) = -k_b(s) v_b(t) \tag{3.10}$$

Finally, creeping flow gives rise to the condition

$$\dot{v} = 0 \tag{3.11}$$

which is to say that changes in speed happen instantly and the total momentum of the system is always zero.

$$\int_0^\infty F_a \, dt = \int_0^\infty F_r \, dt \tag{3.12}$$

$$\int_0^\infty k_b(s(t)) v_b(t) \, dt = -\int_0^\infty k_w(s(t)) v_w(t) \, dt \tag{3.13}$$

In order to facilitate our calculations we need to make an approximation to remove the shape dependence on time. Since the stroke is periodic we will consider only one cycle and divide time as follows.

$$\text{Phase 1, } 0 \leq t \leq T_1$$

$$\text{Phase 2, } T_1 \leq t \leq T_2$$

$$\text{Phase 3, } T_2 \leq t \leq T_3$$

$$\text{Phase 4, } T_3 \leq t \leq T_4$$

We observe from the stroke in Figure 3.1 that the motion in phase 2 and 4 is symmetrical and therefore cannot result in any motion of the bulk of the body. Thus we will look at only phases 1 and 3 of the stroke and assume the shape parameters to be constant during the entire phase. For phase 1 we have the following equation

$$\int_0^{T_1} k_{b_1} v_{b_1}(t)\, dt = -\int_0^{T_1} k_w v_{w_1}(t)\, dt \tag{3.14}$$

and for phase 3 we have

$$\int_{T_2}^{T_3} k_{b_2} v_{b_2}(t)\, dt = -\int_{T_2}^{T_3} k_w v_{w_2}(t)\, dt \tag{3.15}$$

where v_{w_1} and v_{w_2} are the speeds of the wing during the first and third phases respectively. Rearranging these equations yields,

$$\int_0^{T_1} v_{b_1}(t)\, dt = -\frac{k_w}{k_{b_1}} \int_0^{T_1} v_{w_1}(t)\, dt \tag{3.16}$$

$$\int_{T_2}^{T_3} v_{b_2}(t)\, dt = -\frac{k_w}{k_{b_2}} \int_{T_2}^{T_3} v_{w_2}(t)\, dt \tag{3.17}$$

Since the travel of the wing is always the same distance,

$$\int_0^{T_1} v_{w_1}(t)\,dt = \int_{T_2}^{T_3} v_{w_2}(t)\,dt \tag{3.18}$$

We will define this total travel distance to be d_w. Next we let,

$$d_{b_1} = \int_0^{T_1} v_{b_1}(t)\,dt \tag{3.19}$$

$$d_{b_2} = \int_{T_2}^{T_3} v_{b_2}(t)\,dt \tag{3.20}$$

which gives the following two relationships

$$d_{b_1} = -\frac{k_w}{k_{b_1}} d_w \tag{3.21}$$

$$d_{b_2} = -\frac{k_w}{k_{b_2}} d_w \tag{3.22}$$

using our claim of strict monotonicity of $k(s)$ in s we have

$$k_{b_2} > k_{b_1} \tag{3.23}$$

which implies

$$|d_{b_2}| < |d_{b_1}| \tag{3.24}$$

which is to say that the bulk of the body travelled less distance backward in phase 3 of the stroke than it did forward in phase 1. Thus the robot will achieve net motion.

3.3 Mechanical Design

In this section we present our design and implementation considerations for the construction of a prototype to test our hypothesis from the previous section. Working in the low Reynolds number environment presents design challenges that are not

encountered in most robot locomotion problems.

The most important consideration we had in developing the design was to achieve an adequately small Reynolds number. Since it was not feasible at this stage to build a prototype the size of an amoeba we needed to scale our robot while maintaining the low Reynolds number environment. This meant moving slowly through a very viscous fluid, and maintaining the smallest possible characteristic length.

3.3.1 High Viscosity Fluid

In order to create a low Reynolds number environment in which to test our macroscopic robot, we needed a very high viscosity fluid. We considered using racing oil. Although this oil has the appropriate viscosity at room temperature, it is a hazardous material and thus would be very difficult to store and work with. For this reason we chose to use polydimethylsiloxane (PDMS). This compound was ideal for our purposes because it has a specific gravity of 0.977 and a viscosity of $100,000cSt$. Which means its density is almost exactly the same as water, but it is 100,000 times more viscous. In addition it is not known to react with any other compound and is not hazardous to work with in any way. It also has a very high electrical impedence which allows electronic devices to be submerged without the risk of a short-circuit.

We used a large rectangular tank to hold the PDMS. When the PDMS was in the tank it was just over $21cm$ deep. Figure 3.3 shows the tank with the PDMS housed inside the frame we built for support.

3.3.2 Drive System

Given the viscosity of the fluid, we now had to design the robot such that we could achieve an appropriate Reynolds number.

By using Equation (1.1) we were able to make some rough calculations for the parameters based on a viscosity of 100,000 cSt and a speed of 1 mm/s. Equa-

Figure 3.3: Tank to hold PDMS

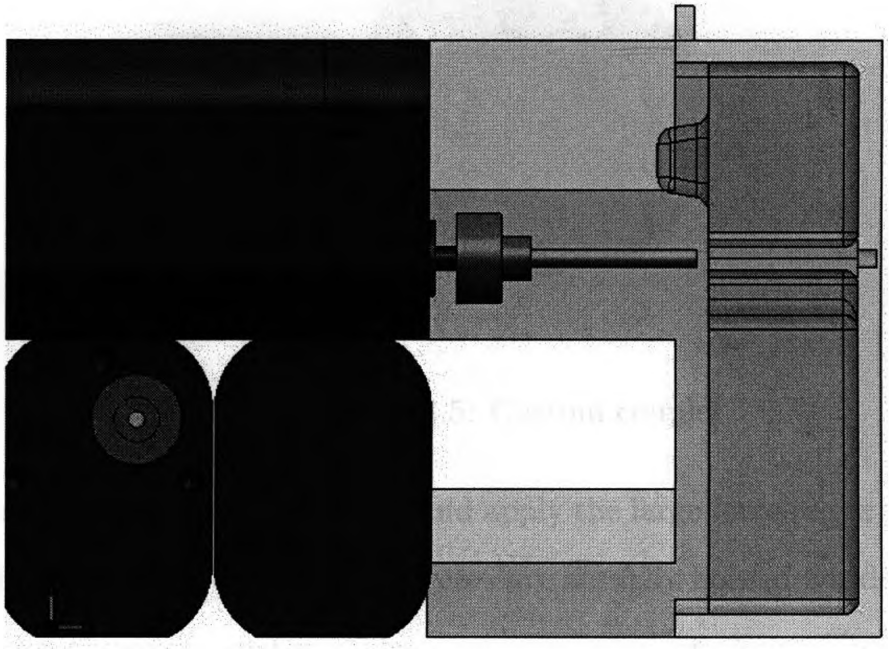

Figure 3.4: Drive Assembly

tion 3.25 shows the relationship between the Reynolds number and the characteristic length based on these parameter values. We note that 1 mm/s= 10^{-3} m/s and $100,000cSt = 10^{-1}m^2/s$.

$$Re = \frac{10^{-3}}{10^{-1}}L \tag{3.25}$$

For our purposes we decided to attempt to achieve a Reynolds number on the order of 10^{-3}. We can see from Equation (3.25) that this requires a characteristic length of $10cm$. The main constraint on the size of the body was the length of the motors.

The drive system for this robot consisted of four gear motors each of which turned a threaded rod. A coupling nut was glued to each wing and thus the threaded rod could change the position of the wing. The drive assembly is shown in Figure 3.4.

The motors chosen for this robot were made by Buehler Motors. They have a gear ratio of 100:1 and a unique form factor. The high gear ratio was necessary in

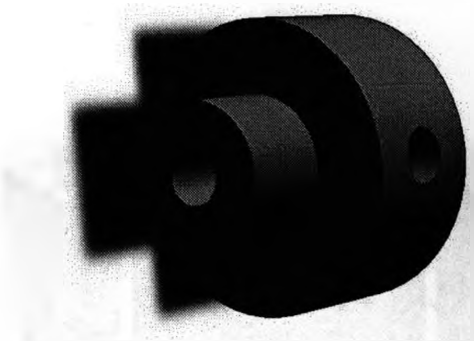

Figure 3.5: Custom coupler

order to move as slowly as possible, and apply the large force required to push against the highly viscous fluid. Indeed the gears are actually housed beside the motor which allowed for the entire motor package to only be 40mm long. This is in contrast to most gear motors which have planetary gears located co-axially with the motor and are therefore much longer. In order to maintain the size of the robot and thus the Reynolds number, the shorter motors were essential because the entire robot had to be scaled by the length of the motors. Using regular gear motors would have increased the characteristic length of the robot by nearly a factor of two.

To connect the motors to the threaded rods we designed a custom coupler (Figure 3.5). The rods were welded to one side of the coupler and then a set screw was used to hold them onto the motor shaft.

3.3.3 Main Body

We chose to build the body and wings using a fixed deposition machine, which allowed us to easily produce intricate detail designed in a CAD package. When we designed the main body of the robot we decided to make it slightly positively buoyant. This would allow most of the robot to be submerged and therefore interact with the fluid, but would eliminate the need for active depth control.

The main body for this robot consisted of a compartment for the motors as

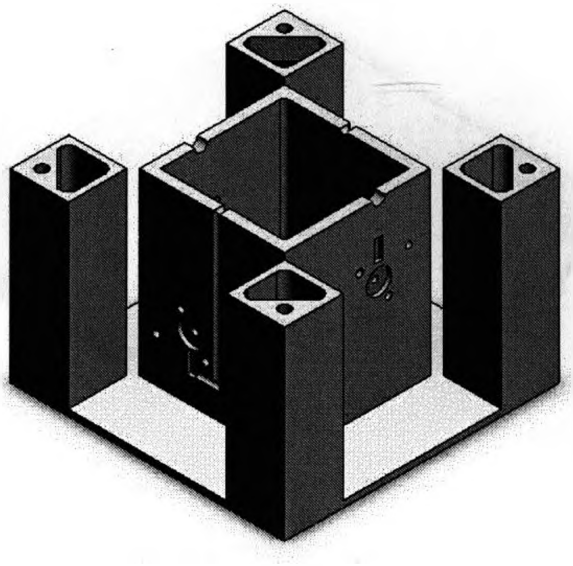

Figure 3.6: Main housing

well as a guide for the wings. We chose the height of the housing to fit the motors. The only real constraint on this dimension was that it had to be no greater than the characteristic length. Since we were very concerned with size we chose not to mount batteries on board the robot. Not only would batteries have required enough space for them to fit, they would have added significant weight which would force us to make the robot much larger in order to maintain buoyancy.

The motor compartment was designed to be sealed separately from the rest of the robot. In the case of a leak, this would allow for the robot to sink without damaging the motors. The dimension of one side of the square with all of the wings retracted was 130mm. Each wing was able to extend 22mm. Our expectation was that this would allow for a significant enough shape change to effect motion.

The pillars in each corner were designed to be completely sealed. Besides the fact that they acted as a guide for the wings, this allowed the robot to maintain some buoyancy even if it started to leak. Both the main housing (Figure 3.6) and the top (Figure 3.7) were designed to have small switches mounted on them to use for wing control. In the case of the top this meant that there needed to be tabs which extended

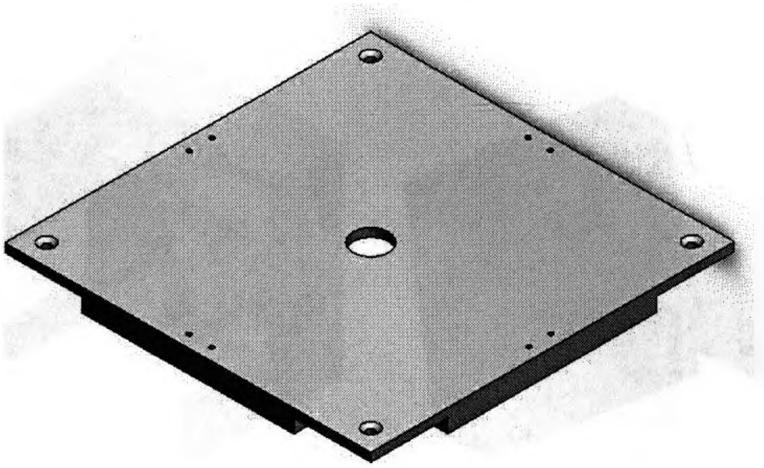

Figure 3.7: The top

downwards from the top that could hold the buttons and catch corresponding tabs on the wings. Figure 3.7 also shows a hole in the centre of the top. This was for a snorkel. There were two reasons why a snorkel was necessary: to act as a conduit for the wires, and to equalize the pressure. The latter point had important implications on our design. Our swimming stroke required the robot to change its volume. We knew that we were not able to seal the robot well enough or construct it strong enough to allow it to change its internal pressure. Therefore the only alternative would have been to make the motor compartment large enough to provide enough buoyancy for the entire robot to float, and allow the fluid to pass freely into and out of the wings. However, we felt that creating vents in the body for the fluid to pass through would cause unintentional propulsion when the fluid moved in or out. If true, this would completely change the dynamics of the system, and was therefore undesirable. A snorkel avoids this problem.

3.3.4 Wings

The wings were the most intricate part of the design. Because of our size constraints the drive screws could not be positioned centrally on the wing. Therefore there was a net moment across both dimensions of the wing as it moved. Thus in our design we

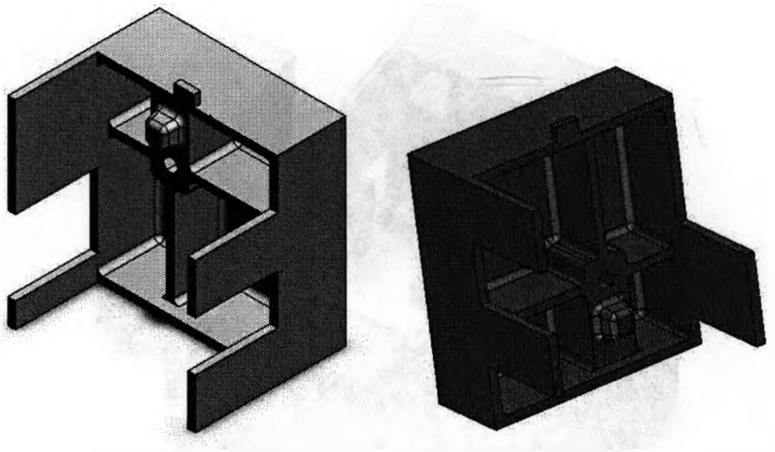

(a) Wing 1 (b) Wing 2

Figure 3.8: Interlocking wings

were very concerned about the wings binding during travel and potentially breaking. To avoid this problem we designed interlocking fingers on each wing so that the wings were always being guided by the other wings. This is shown in Figures 3.8 and 3.9.

The other major challenge concerning the wings was sealing the robot. Since we were using a square design, conventional sealing techniques such as o-rings would be complicated and difficult. On account of the extremely high viscosity of the fluid we chose to not use a sealing mechanism for the wings. We simply designed the wings without any clearance. Once the robot had been constructed the wings were sanded down until they could just barely fit. The idea was that they would leak but very slowly, hopefully allowing enough time to conduct the experiment before the robot sank.

3.3.5 The Controller

Control for this robot was performed on a Motorola HCS12 micro-controller board. Two dual h-bridge motor drives were used, so independent control of each motor was possible. Although this was not necessary for the swimming stroke described above, the intention was to investigate other sequences if this one was successful.

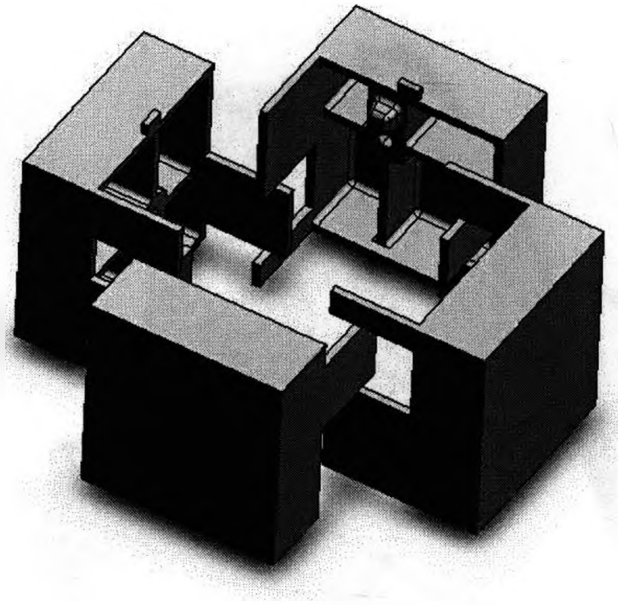

Figure 3.9: Wing assembly

Push-button switches were placed at either end of the wing's travel so that the fully extended and fully retracted positions could be detected. The board is shown in Figure 3.10.

3.4 Observations

The robot floated with the top just above the surface of the fluid, as designed. In addition, the wings moved slowly enough that the Reynolds number for the system was on the order of 10^{-4}, which is consistent with our assumption of creeping flow.

The observed stroke can be seen in Figure 3.11. During the swimming stroke, as the first wing extended, the buoyancy was unbalanced and the robot began to rise on one side. What appeared to be happening is that instead of the wing displacing some volume of PDMS, the robot was rising out of the fluid and therefore causing very little motion in the surrounding fluid. This effect can be better seen in Figure 3.12 which shows shows the robot at the end of phase 3 of the stroke, before it has had time to settle back into the fluid.

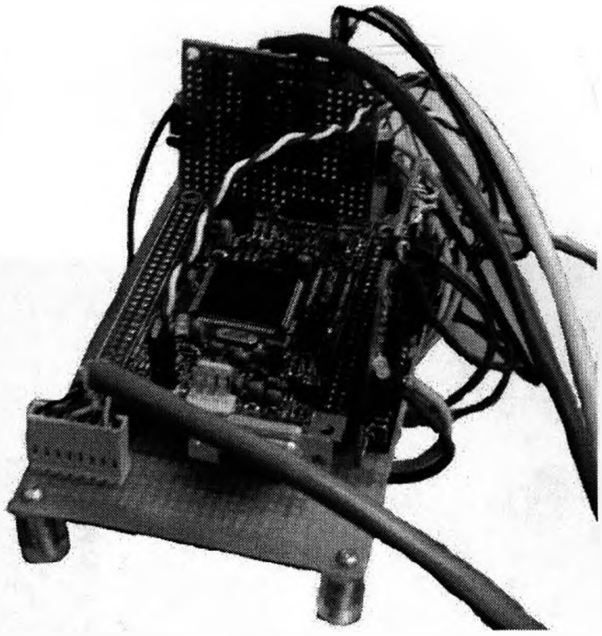

Figure 3.10: Motor control board

The swimming cycle was repeated continuously for five days. There was no sign of a change in position or orientation at the end of the experiment. The robot had some fluid inside but was still floating.

Another problem which we observed concerned the tether which was used to power the motors and read signals from the switches. This cable had a total of 24 wires and was therefore so resistant to deformation that it appeared to be the most significant factor determining the position of the robot. Indeed after 5 days of swimming with no apparent results, simply moving the cable a short distance would cause the robot to move and rotate. Also, in an attempt to circumvent this obstacle, we allowed some slack in the cable with the intention reducing or eliminating the tension. What we found in this case was the weight of the cable would simply tip over the robot, and after about 5 minutes the robot would be upside down.

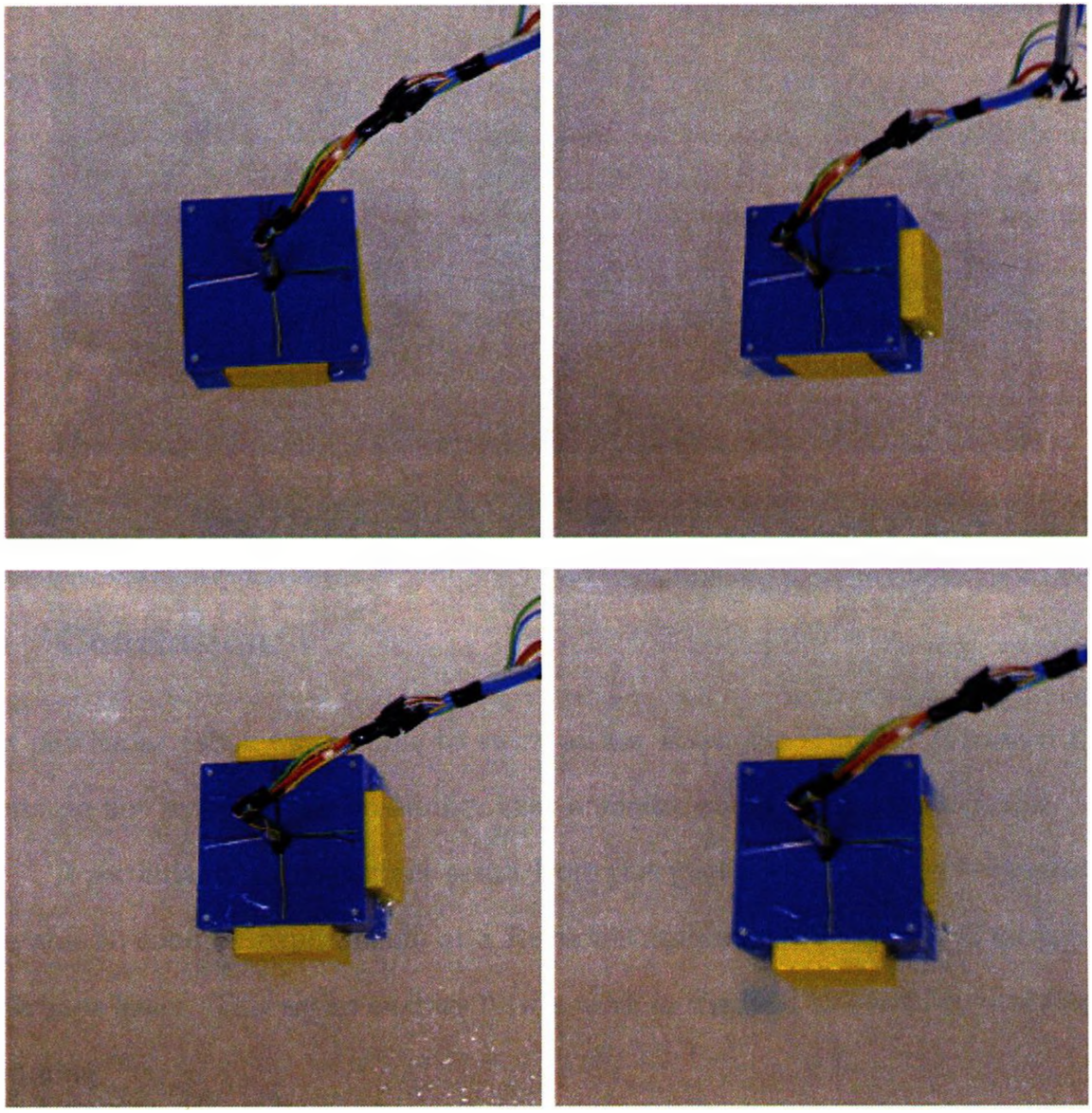

Figure 3.11: Observed swimming stroke

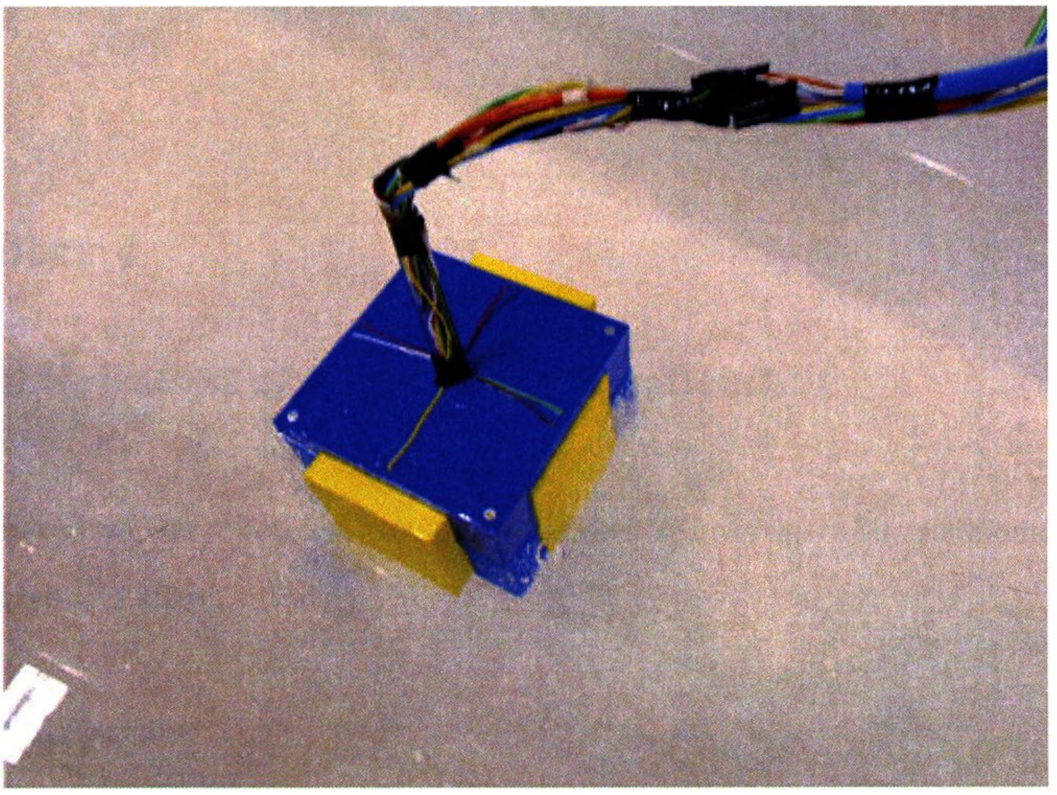

Figure 3.12: Effect of unbalanced buoyancy

3.5 Conclusion

This particular robot was unable to swim at low Reynolds number. However, these results do not preclude the possibility that a similar robot could be successful.

A secondary but important result from this portion of the project was that we were able to conduct experiments at a Reynolds number characteristic of an amoeba or perhaps lower. This setup enables future work in the field of low Reynolds number swimming.

Chapter 4

Characterization of Force-Shape Relationship

Based on the robot test results we decided to investigate the relationship between force and shape.

4.1 Purpose

The purpose of this experiment was to investigate the cause of the negative results from our prototype swimmer. In addition we hoped to characterize a shape parameter which could be used to predict the force that would be experienced by a similarly shaped object at low Reynolds number. This is important to this project because if found it would complete the model presented in section 3.2 which could then be used to design and analyze the motion control of a shape changing, swimming robot.

4.2 Apparatus

The main portion of the apparatus was a device to push objects through the PDMS and measure the force required. For this experiment we built a sealed enclosure with an actuator mounted inside. On the end of the actuator we mounted a piezo-electric compression sensor. This was attached to a rod which extended through a seal into the PDMS. The end of this rod was threaded.

To control the experiment as well as record the data, we used a Texas Instruments MSP430 based microcontroller board.

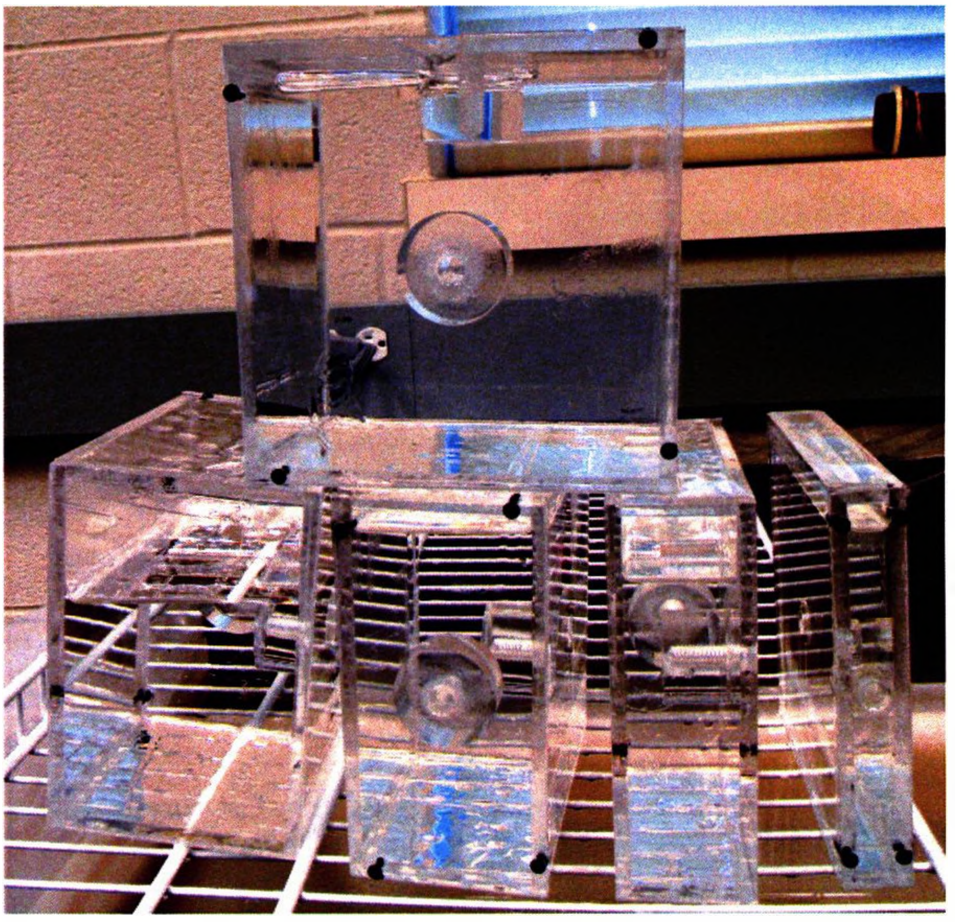

Figure 4.1: Blocks used in pushing experiment

Since our robot was based on a cube, we chose to investigate the relationship between force and the two dimensions of a rectangular prism. We built 6 blocks. Each block had 2 six inch square sides, but the third dimension differed by one inch in each block. This is to say we had a 6 inch cube, a block whose dimensions were 6x6x5 inches down to a block whose dimensions were 6x6x1 inches. The blocks are shown in Figure 4.1.

Each block was built from clear plastic and was hollow. One side was removable so that the block could be filled with the PDMS, in an effort to curb possible problems arising from buoyancy. A threaded hole was added to the six inch face and in the case of the non cubic blocks a hole was added to the smaller face. This was done to facilitate a connection between the block and the actuator. The apparatus pushing

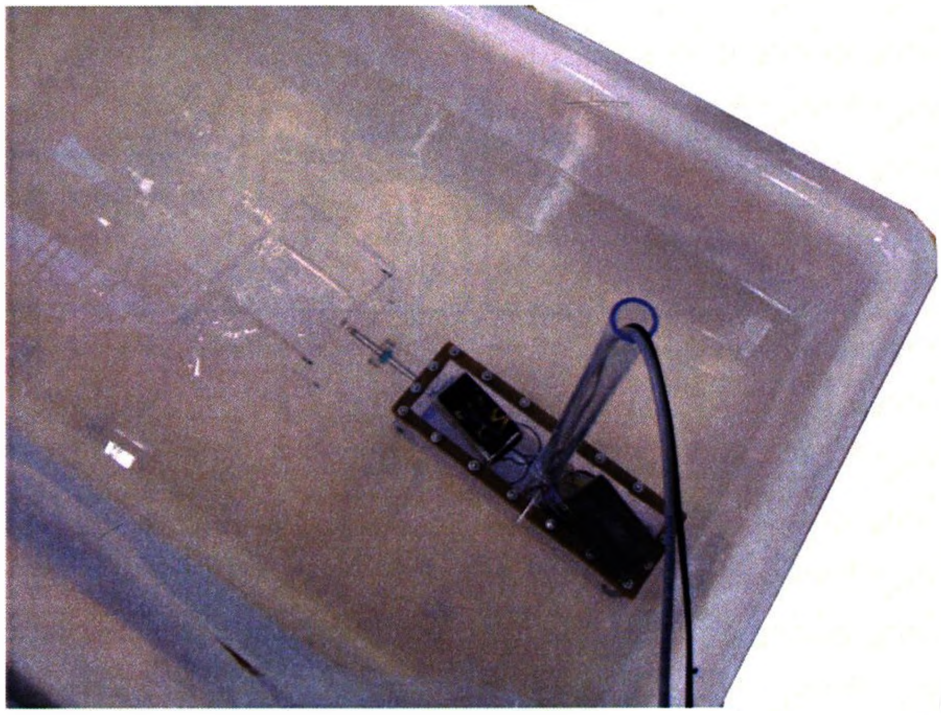

Figure 4.2: Pushing apparatus with 5 inch block

the 5 inch block is shown in Figure 4.2.

4.3 Method

The overall procedure for this experiment was to push the blocks through the PDMS at a constant speed and measure the required force. We chose to perform these tests in two orientations. The first trials were conducted with the normal of the six inch square side of each block parallel to the direction of travel. We will refer to this configuration as parallel (Figure 4.3(a)). Secondly, we ran the experiment with the normal of this face perpendicular to the direction of travel. We will refer to this configuration as perpendicular (Figure 4.3(b)).

We chose to run the experiment with the actuator powered by seven different voltages. This was done because the relationship we were ultimately looking for was between force and speed parametrized by shape and the speed of the actuator is dependent on the voltage.

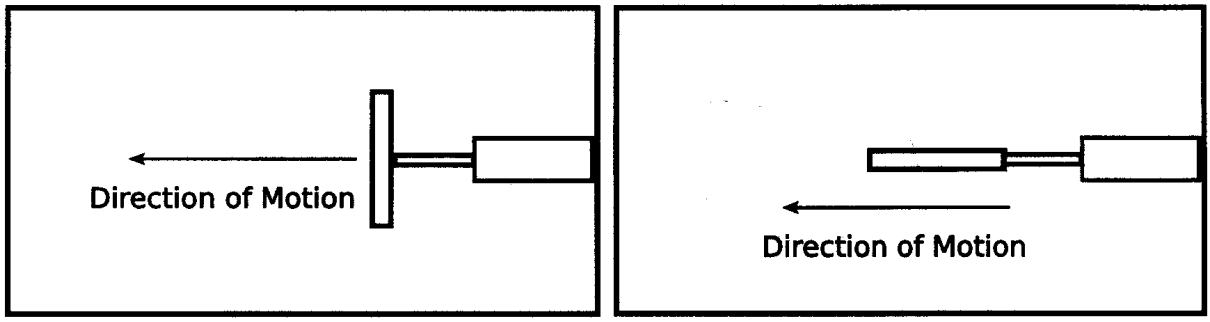

(a) Parallel Orientation (b) Perpendicular Orientation

Figure 4.3: Block orientation for trials

For each integer valued voltage from 6V-12V we ran two trials in both the parallel and perpendicular configurations. Initially the perpendicular trials were run with the narrow face of the block parallel with the surface of the PDMS. The trials were then run a second time with the six inch square face parallel with the surface of the PDMS.

4.4 Observations

During the trials air bubbles were moving around inside of the blocks. We attempted to add more PDMS but it was not possible to eliminate the bubbles completely. These bubbles moved in an unpredictable manner which caused some rotation of the blocks during the trials. This was a particular problem in the lower voltage trials because the duration of the trial was longer.

Between each block configuration it was necessary to completely remove the apparatus from the PDMS in order to change the block or reorient it. When the apparatus was removed from the fluid it was placed on a wire shelf above the tank. This allowed the fluid which was still on the plastic to slowly drain back into the tank. The draining caused a large number of bubbles to form in the fluid (Figure 4.4) which would remain visible for more than an hour. In addition, when the apparatus was placed back into the fluid large bubbles would form all around it. These bubbles

Figure 4.4: Bubbles which formed between trials

would rise to the surface within several minutes, but small bubbles would remain and would cling to the plastic blocks. These bubbles would not disappear in less than two hours. Therefore it was necessary to run the trials with many of the bubbles present due to time constraints. It is possible that the bubbles had an effect on the viscosity or the density of the fluid. However, we did not take this into account in our models and thus it is a possible source of error.

We also observed an extremely strong suction force between flat surfaces that were close or touching. Indeed it was difficult to lift the apparatus out of the tank even though we had glued small feet on the bottom.

4.5 Results and Conclusions

We begin by establishing a method for collapsing a data set from a trial into a single speed and force pair. Figure 4.5 shows a representative trial. The position of the block is clearly linear in time, thus we may consider only the slope of this line which

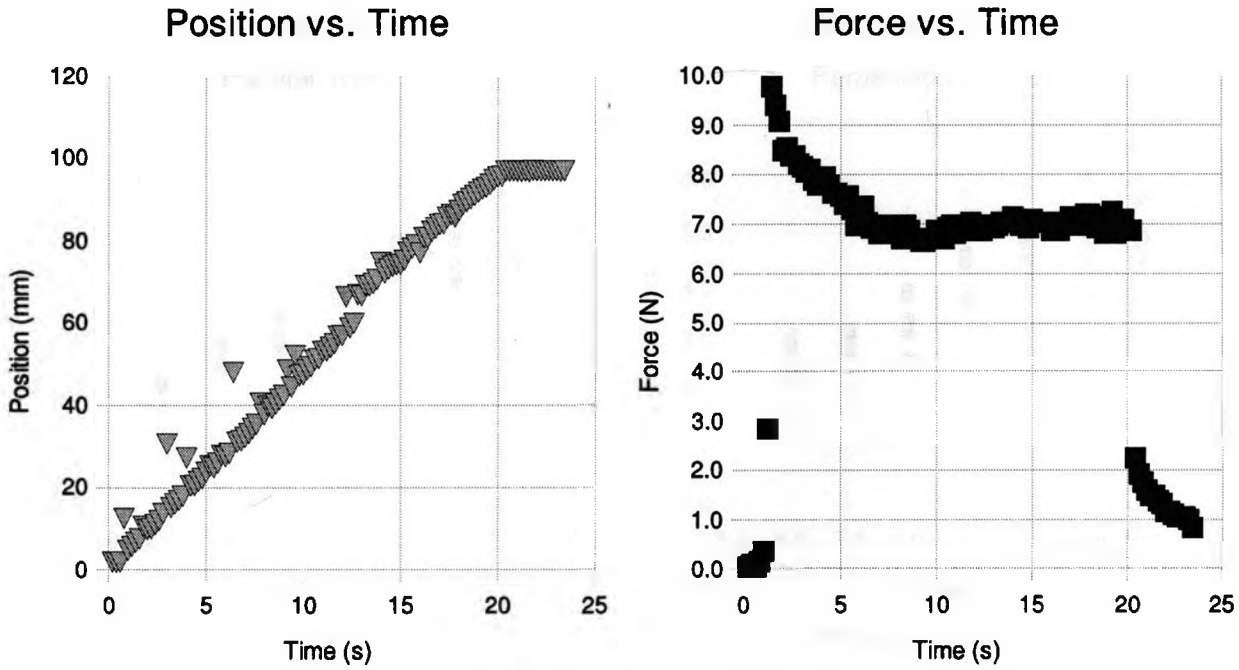

Figure 4.5: Position and force in time

gives us a constant speed. The force has an asymptotic relationship with time. We see a transient period as it decays to a steady state value. However, from the position plot we can clearly see that this force transient is not due to acceleration since the block changes speed almost instantly. We know from creeping flow that force is linear in speed, and thus for constant speed we expect only a constant force. Therefore we conclude that the force transient is related to other interactions perhaps due to the proximity of the block to the pushing apparatus, or proximity to the surface. In any case, we are only interested in steady state value and so for the purposes of our analysis we remove these other effects by clipping the transient period from the data and taking the mean value during the period of steady state.

We now show the relationship between measured speed and applied voltage. The results for the two orientations are shown in Figure 4.6. These results show that speed is linear in voltage up to 11V. For the 11V and 12V grouping the relationship breaks down. One possible reason for this is that the motor drive circuit reached its

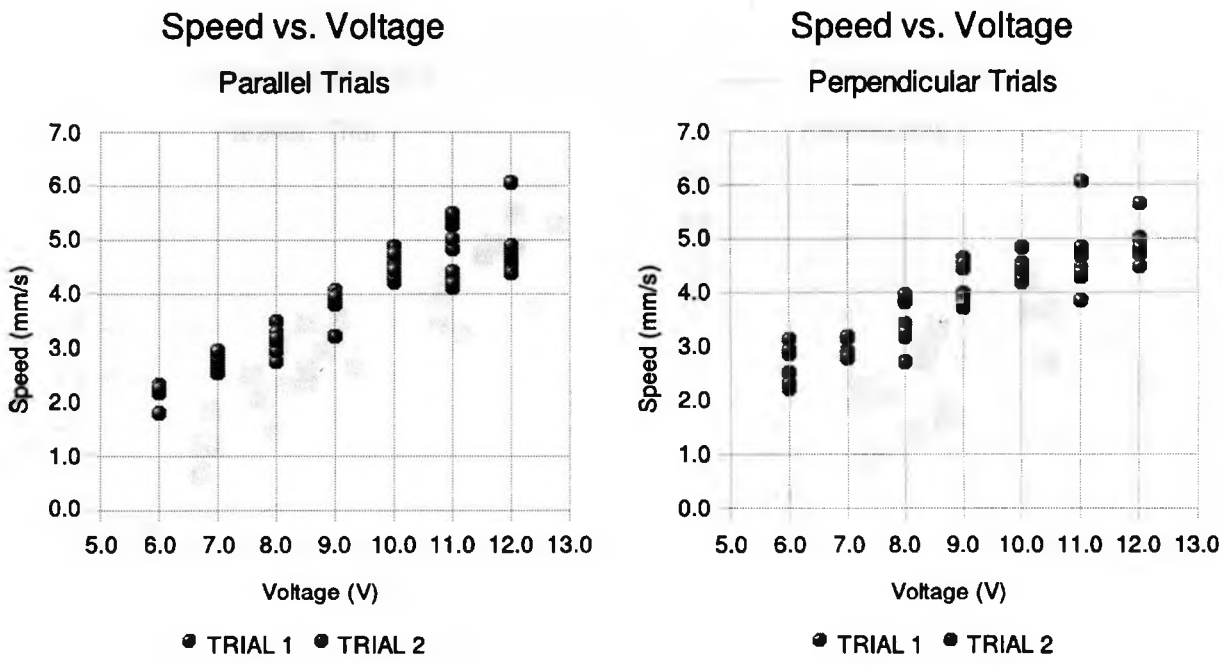

Figure 4.6: Speed-Voltage Relationship

saturation current. We therefore chose to only look at results from 6V-10V where we had the linear relationship. This way voltage would be interchangeable with speed on other plots.

One of the important results of this work was that we confirmed force was proportional to speed as shown in Figure 4.7. This is another indication that we were operating at a sufficiently low Reynolds number to justify the creeping flow approximation.

The results from the parallel trials are shown in Figure 4.8. We see from these plots that there is no trend relating the shape changes to the force. This may indicate that changing the dimension in the axis parallel to the direction of motion has no effect on force. However, later results bring this conclusion into question.

The initial results of the perpendicular configuration can be seen in Figure 4.9. Although these results do show variation with the shape, there is no clear trend. At a minimum these results defy our assumption of strict monotonicity in shape.

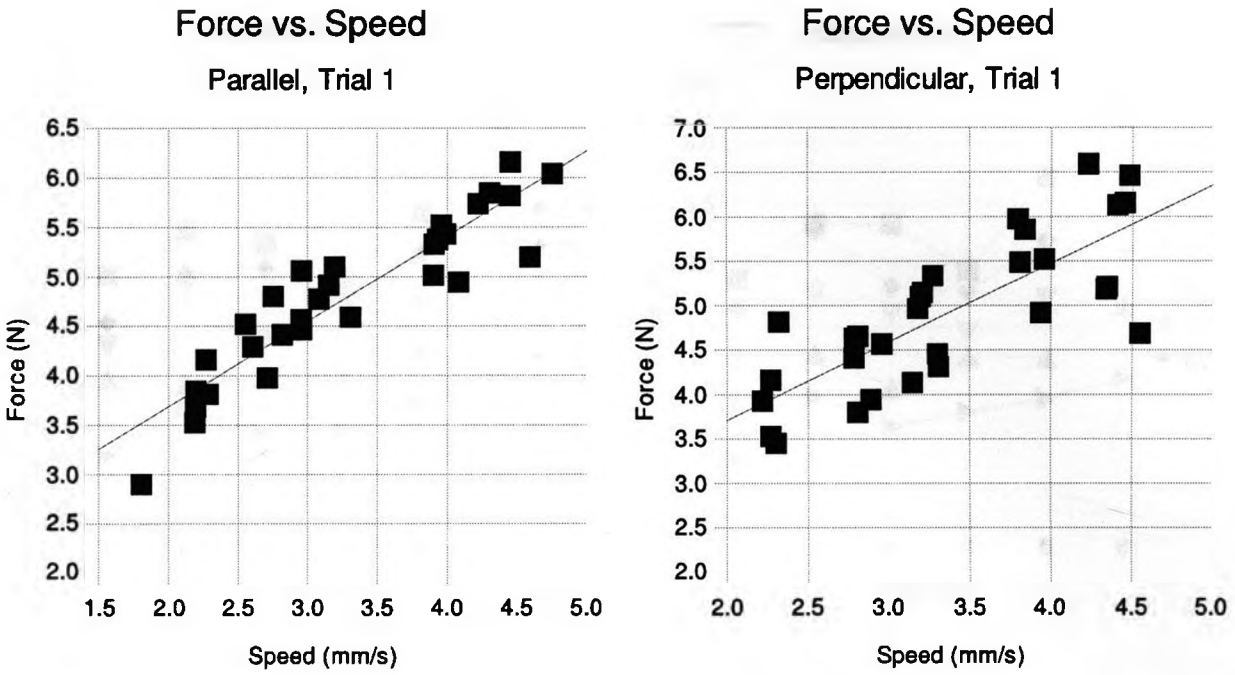

Figure 4.7: Force-Speed relationship for parallel and perpendicular trials

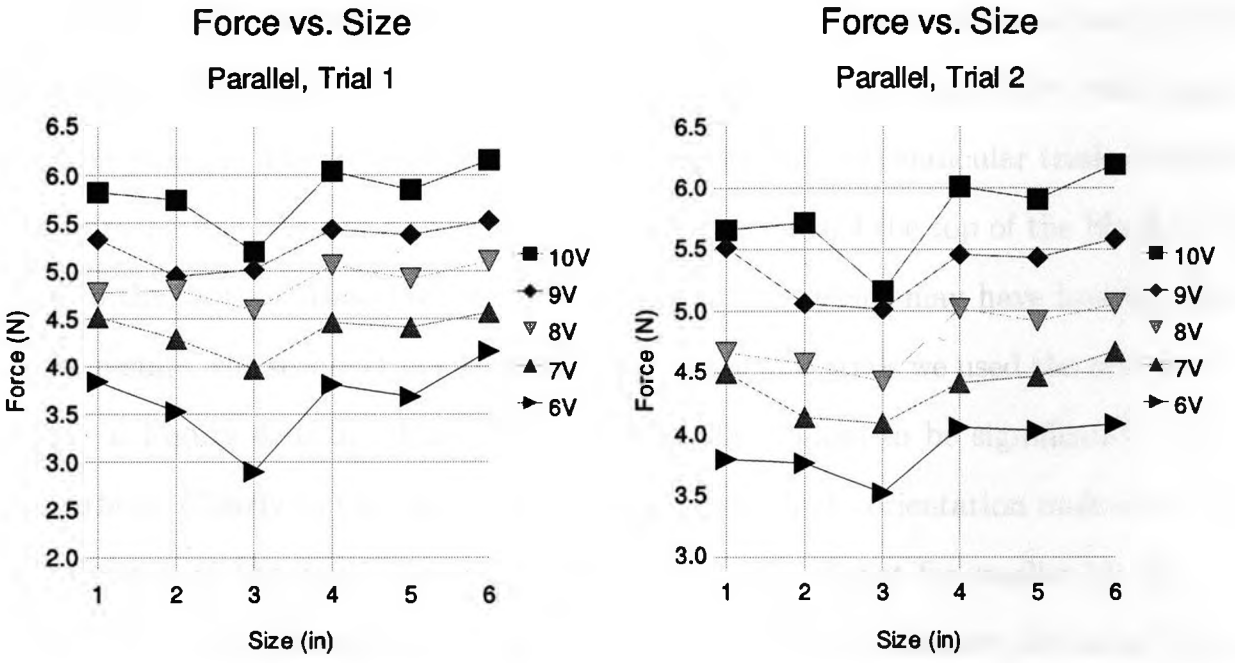

Figure 4.8: Force-Size relationship for parallel trials

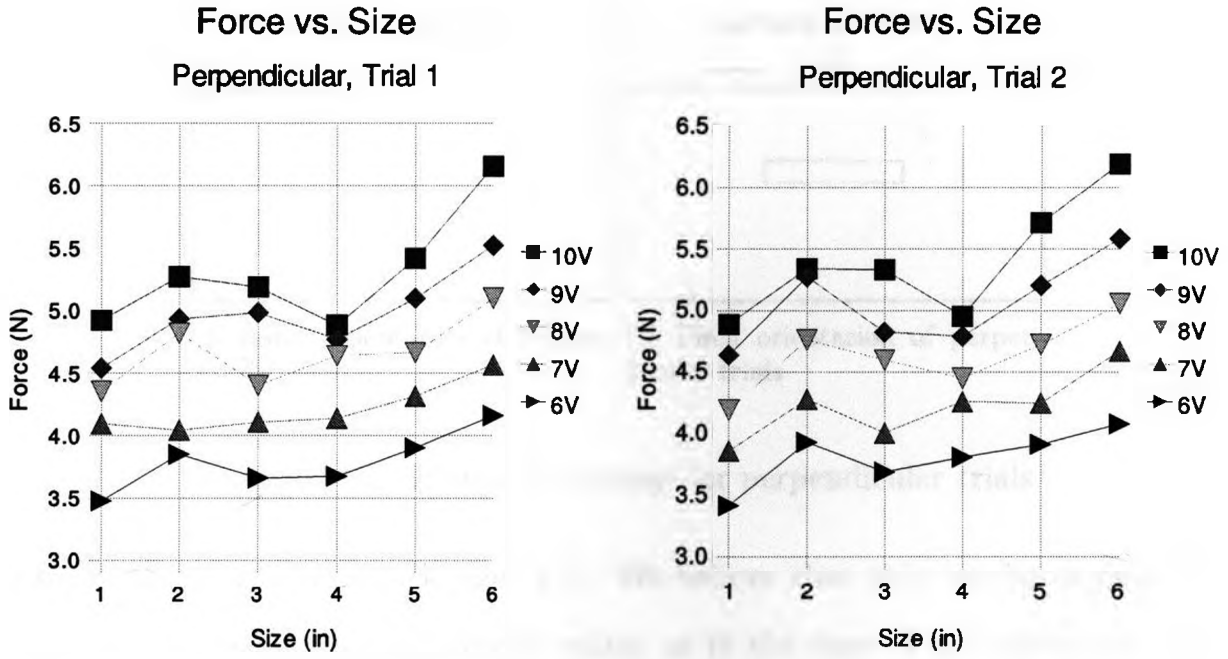

Figure 4.9: Force-Size relationship for initial run of perpendicular trials

This would seem to indicate that changing the dimension in the axis perpendicular to the direction of motion does not alter the drag force in a predictable way. However, we were not prepared to accept this conclusion based on the theoretical background presented in section 3.1. Therefore we chose to run the perpendicular trials again with one change. The initial orientation we used for the perpendicular trials is shown in Figure 4.10(a). As can be seen in the figure, this caused the top of the block to be close to the surface. Based on our intuition that the surface may have had an effect on the results, the second time we ran the perpendicular trials we used the orientation shown in Figure 4.10(b). This allowed the smaller blocks to be significantly below the surface. Clearly in the cases of the 5 and 6 inch blocks orientation makes little or no difference to the depth, but the effect would be significant for smaller blocks.

The results from the second run of the perpendicular trials are shown in Figure 4.11. These results show a relationship much closer to the one we were expecting. Between block sizes 2-4 we clearly have strict monotonicity. This relationship appears

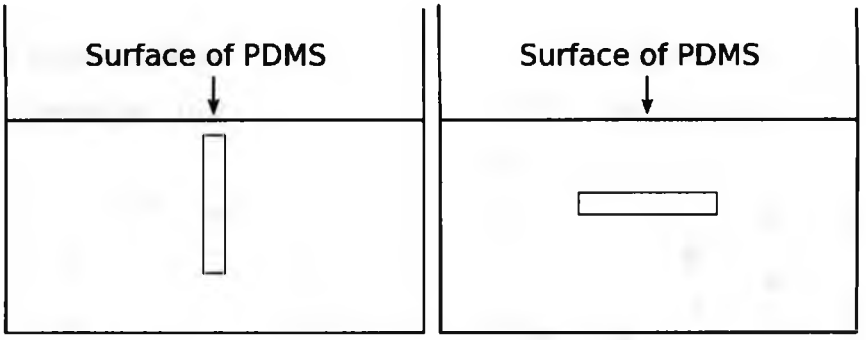

(a) Initial orientation of perpendicular trials

(b) Final orientation of perpendicular trials

Figure 4.10: Orientation change for perpendicular trials

to break down between block sizes 1-2. We believe that this can be explained by the force approaching an asymptotic value, as in the case of the edgeways disk in Equation (3.5). In our case as the blocks become smaller the characteristic length becomes the other dimension which is fixed. Thus, it follows that our results should asymptotically approach the value of an infinitesimally thin six inch square moving edgeways. Furthermore, it is likely that such small changes are lost in the accuracy of our piezo-electric compressive force sensor.

These results lead us to the conclusion that although our experiment did exhibit properties consistent with our creeping flow approximation, there were other effects present which interfered with the results. One probable cause was the proximity of the blocks to the surface in certain trials. This condition renders the results of the parallel trials inconclusive.

Overall we conclude that the relationship between force and the dimension perpendicular to the direction of motion is monotonic. Furthermore, in order to maintain this relationship, the blocks must be far enough from the surface so as not interact with it. The results from this chapter also have implications for the results of the preceding chapter. We may now conclude that in order to build a robot capable of swimming at low Reynolds number, it must be submerged completely. However, we may also conclude that the results of this experiment are consistent with our assertion

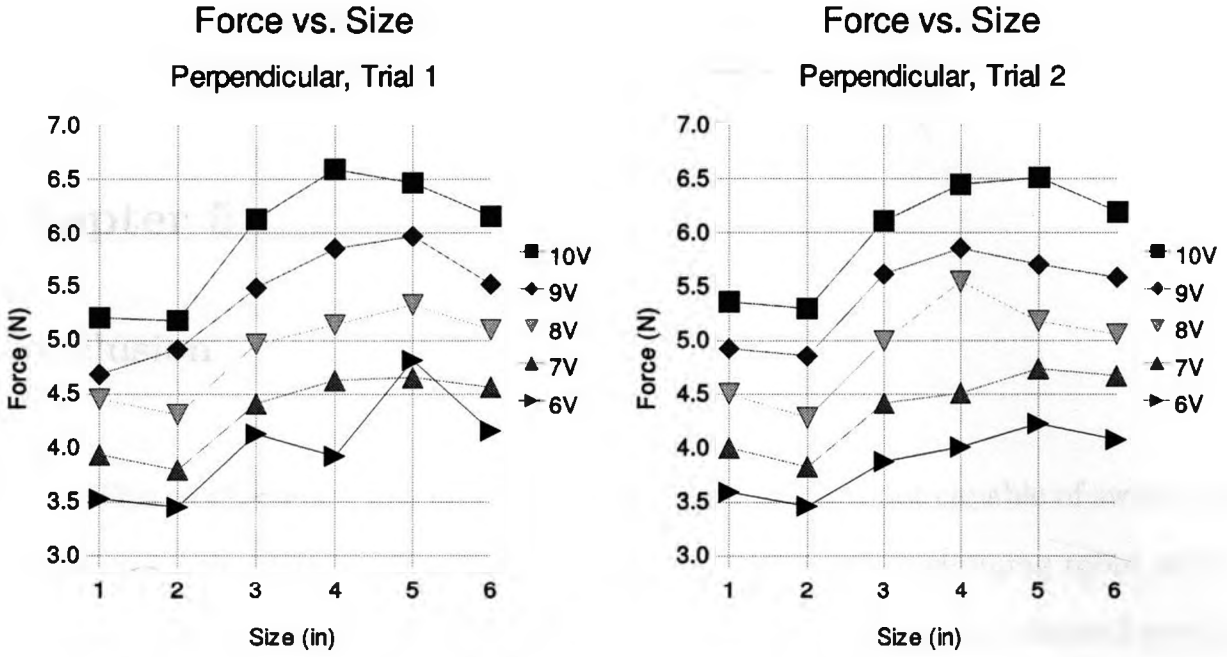

Figure 4.11: Force-Size relationship for second run of perpendicular trials

of strict monotonicity as presented section 3.2, and therefore it is likely that a new implementation using depth control to stay well below the surface would be likely to achieve net displacement by swimming.

Chapter 5

Conclusion

This work was motivated by the goal of building a robot capable of swimming on a microscopic scale by changing its shape. A microscopic swimming robot would have many possible applications. In particular, uses in medicine have inspired several projects in the field. We began our investigation by attempting to design a deformable robotic sphere. In this portion of the work we developed a method of matching a tensegrity structure to a deforming sphere. We also found that shape memory alloy coils can be used as actuators for implementation of a deforming tensegrity sphere. Due to the complexity of a tensegrity structure we chose to pursue a simpler design for a prototype. We proposed a model for a box-shaped robot, and we built a prototype and tested it in very high viscosity polydimthylsiloxane. Although the results of this test did not show any displacement of the robot, we were able to achieve a low Reynolds number test environment which will be useful in future work. Finally, we built an apparatus to measure the drag force experienced by objects being pushed through our high viscosity fluid, in order to investigate the negative results of the robot. Based on experiments run using this apparatus we were able to show that a deformable box-shaped robot can swim if it is far enough from the surface. We used this result to suggest design modifications for a second generation prototype.

5.1 Future Work

In future work we plan to attach our prototype robot to our pushing apparatus and measure drag forces as the robot changes shape. We believe this experiment will show that this prototype is capable of locomotion when it is far enough from the surface.

The next logical progression would be to build a second prototype of the same design which has an on-board power source. Of course there will be additional complications in this design because a second prototype would need active depth control which could be could prove to be a prohibitive constraint. In addition there would still be the problem of pressure equalization due to the robot changing its volume. This problem could be overcome by a small snorkel which allows air to pass into and out of the robot.

We also foresee this robot exhibiting an elegant control problem. It should be the case that this design of robot is capable of turning. However, the rotation is likely to be coupled with a translation. If we consider a space which represents all possible shape configurations, this rotation is likely to induce an interesting operator under which the space is closed. Furthermore, if we consider a space which represents all positions in space with all possible shape configurations (this space would formally be the product of two spaces) we would have a (hopefully invertible) mapping based on the model we presented which would take elements of either space and map them to the other. We note that this mapping would not be bijective, but would have very interesting geometric properties. Using this construction, we would be able to investigate the controllability of the problem as well as introduce metrics which would allow us to define optimal strokes.

References

[1] G. Kosa, M. Shoham, and M. Zaaroor, "Propulsion method for swimming microrobots," *IEEE Transactions on Robotics*, vol. 23, pp. 137–150, February 2007.

[2] G. Kosa, P. Jakab, N. Hata, F. Jolesz, Z. Neubach, M. Shoham, M. Zaaroor, and G. Szekely, "Flagellar swimming for medical micro robots: Theory, experiments and application," *The second IEEE / RAS-EMBS International Conference on Biomedical Robotics and Biomechatronics*, pp. 258–263, October 2008.

[3] G. Kosa, P. Jakab, F. Jolesz, and N. Hata, "Swimming capsule endoscope using static and rf magnetic field of mri for propulsion," *IEEE Conference for Robotics and Automation*, pp. 2922–2927, 2008.

[4] G. Iddan, G. Meron, A. Glukhovsky, and P. Swain, "Wireless capsule endoscopy," *Nature*, vol. 405, p. 417, May 2000.

[5] I. Dabney R. Yarbrough, J. C. McAlhany, N. Cooper, and J. Michael G. Weidner, "Evaluation of the heidelberg ph capsule," *American Journal of Surgery*, vol. 117, pp. 185–192, 1969.

[6] K. McIsaac and J. Ostrowski, "Experimental verification of open-loop control for an underwater eel-like robot," *The International Journal of Robotics Research*, vol. 21, pp. 849–859, 2002.

[7] J. Cortes, S. Martinez, J. Ostrowski, and K. McIsaac, "Optimal gaits for dynamic robotic locomotion," *The International Journal of Robotics Research*, vol. 20, pp. 707–728, 2001.

[8] W. Khalil, G. Gallot, O. Ibrahim, and F. Boyer, "Dynamic modeling of a 3-d serial eel-like robot," in *Proceedings of the 2005 IEEE International Conference on Robotics and Automation*, 2005, pp. 1270–1275.

[9] M. Triantafyllou and G. Triantafyllou, "An efficient swimming machine," *Scientific American*, vol. 272, pp. 64–71, 1995.

[10] J. M. Kumph, "Maneuvering of a robotic pike," Master's thesis, MIT, 2000.

[11] J. Anderson and N. Chhabra, "Maneuvering and stability performance of a robotic tuna," *Integrative and Comparative Biology*, vol. 42, no. 1, pp. 118–126, 2002.

[12] M. Nakashima and K. Ono, *Neurotechnology for biomimetic robots.* Bradford Books, 2002, ch. 16, pp. 309–324.

[13] M. Nakashima, Y. Takahashi, T. Tsubaki, and K. Ono, *Bio-mechanisms of Swimming and Flying.* Springer Verlag, 2004, ch. 7, pp. 79–92.

[14] J. Liu, I. Dukes, and H. Hu, "Novel mechatronics design for a robotic fish," in *IEEE/RSJ International Conference on Intelligent Robots and Systems*, August 2005, pp. 807–812.

[15] R. Mason and J. Burdick, "Experiments in carangiform robotic fish locomotion," in *IEEE International Conference on Robotics and Automation*, vol. 1, 2000, pp. 428–435.

[16] I. Yamamoto and Y. Terada, "Robotic fish and its technology," in *SICE 2003 Annual Conference*, vol. 1, 2003.

[17] J. Yu, M. Tan, S. Wang, and E. Chen, "Development of a biomimetic robotic fish and its control algorithm," *IEEE Transactions on Systems, Man, and Cybernetics, Part B: Cybernetics*, vol. 34, no. 4, pp. 1798–1810, August 2004.

[18] J. Yu, L. Liu, and M. Tan, "Dynamic modeling of multi-link swiming robot capable of 3-d motion," *Proc. of the IEEE Conference on Mechatronics and Automation*, pp. 1322–1327, August 2007.

[19] J. Ayers, C. Wilbur, and C. Olcott, "Lamprey robots," in *Proceedings of the international symposium on aqua biomechanisms*, 2000.

[20] N. Kato, "Control performance in the horizontal plane of a fish robot withmechanical pectoral fins," *IEEE Journal of Oceanic Engineering*, vol. 25, no. 1, pp. 121–129, January 2000.

[21] K. Low and A. Willy, "Biomimetic motion planning of an undulating robotic fish fin," *Journal of Vibration and Control*, vol. 12, no. 12, pp. 1337–1359, 2006.

[22] S. Guo, T. Fukuda, and K. Asaka, "A new type of fish-like underwater microrobot," *IEEE Transactions on Mechatronics*, vol. 8, no. 1, pp. 136–141, March 2003.

[23] T. Fukuda, H. Hosokai, and I. Kikuchi, "Distributed type of actuators by shape memory alloy and its application to underwater mobile robotic mechanism," *Proc. IEEE Int. Conf. Robotics and Automation*, vol. 2, pp. 1316–1332, 1991.

[24] T. Fukuda, A. Kawamoto, F. Ami, and H. Matsuura, "Mechanism and swimming experiment of micro mobile robot in water," *Proc. IEEE Int. Conf. Robotics and Automation*, vol. 1, pp. 814–819, 1994.

[25] T. Fukuda, A. Wamoto, F. Arai, and H. Matsuura, "Steering mechanism of underwater micro mobile robot," *Proc. IEEE Int. Conf. Robotics and Automation*, vol. 1, pp. 363–368, 1995.

[26] B. Behkam and M. Sitti, "Design methodology for biomimetic propulsion of miniature swimming robots," *Transactions of the ASME*, vol. 128, pp. 36–43, March 2006.

[27] T. Yu, E. Lauga, and A. Hosoi, "Experimental investigations of elastic tail propulsion at low Reynolds number," *Physics of Fluids*, vol. 18, 2006.

[28] J. Edd, S. Payen, B. Rubinsky, M. Stoller, and M. Sitti, "Biomimetic propulsion for a swimming surgical micro-robot," in *IEEE IROS*, 2003, pp. 2583–2588.

[29] C. Brennen and H. Winet, "Fluid mechanics of propulsion by cilia and flagella," *Annual Review of Fluid Mechanics*, vol. 9, no. 1, pp. 339–398, 1977.

[30] C. H. Wiggins and R. E. Goldstein, "Flexive and propulsive dynamics of elastica at low Reynolds number," *Phys. Rev. Lett.*, vol. 80, no. 17, pp. 3879–3882, April 1998.

[31] G. J. Hancock, "The self-propulsion of microscopic organisms through liquids," *Proceedings of the Royal Society of London.*, vol. 217, pp. 96–121, 1953.

[32] E. M. Purcell, "Life at low Reynolds number," *American Journal of Physics*, vol. 45, pp. 3–11, January 1977.

[33] L. E. Becker, S. A. Koehler, and H. A. Stone, "On self-propulsion of micromachines at low Reynolds number: Purcell's three-link swimmer," *Journal of Fluid Mechanics*, vol. 490, pp. 15–35, 2003.

[34] Y. Zhang and G. Liu, "Wireless swimming microrobot: Design, analysis, and experiments," *Journal of Dynamic Systems, Measurement, and Control*, vol. 131, 2009.

[35] K. Yesin, K. Vollmers, and B. Nelson, "Modeling and control of untethered biomicrorobots in a fluidic environment using electromagnetic fields," *The International Journal of Robotics Research*, vol. 25, p. 527, 2006.

[36] K. Ishiyama, M. Sendoh, A. Yamazaki, M. Inoue, and K. I. Aarai, "Swimming of magnetic micro-machines under a very wide-range of Reynolds number conditions," *IEEE Transactions on Magnetics*, vol. 37, pp. 2868–2870, July 2001.

[37] K. Ishiyama, M. Sendoh, A. Yamazaki, and K. I. Arai, "Swimming micromachine driven by magnetic torque," *Sensors & Actuators: A. Physical*, vol. 91, no. 1-2, pp. 141–144, 2001.

[38] A. Yamazaki, M. Sendoh, K. Ishiyama, T. Hayase, and K. Arai, "Three-dimensional analysis of swimming properties of a spiral-type magnetic micromachine," *Sensors and Actuators A*, pp. 103–108, 2003.

[39] K. Kikuchi, A. Yamazaki, M. Sendoh, K. Ishiyama, and K. I. Arai, "Fabrication of a spiral type magnetic micromachine for trailing a wire," *IEEE Transactions on Magnetics*, vol. 41, no. 10, pp. 4012–4014, 2005.

[40] R. Dreyfus, J. Baudry, M. Roper, M. Fermigier, H. Stone, and J. Bibette, "Microscopic artificial swimmers," *Nature-London*, vol. 7060, p. 862, October 2005.

[41] M. Kulic, R. Thaokar, and H. Schiessel, "Twirling DNA rings-swimming nanomotors ready for a kickstart," *Europhysics Letters*, vol. 72, no. 4, pp. 527–533, November 2005.

[42] M. J. Lighthill, "On the squirming motion of nearly spherical deformable bodies through liquids at very small Reynolds numbers," *Communications on Pure and Applied Mathematics*, vol. 5, pp. 109–118, 1952.

[43] J. Blake, "Self propulsion due to oscillations on the surface of a cylinder at low Reynolds number," *Australian Mathematical Society Bulletin*, vol. 5, pp. 255–264, 1971.

[44] S. D. Kelly and R. M. Murray, "The geometry and control of dissipative systems," *Proceedings of the 35th Conference on Decision and Control*, 1996.

[45] I.-M. Chen, H.-S. Li, and A. Cathala, "Mechatronic design and locomotion of amoebot-a metamorphic underwater vehicle," *Journal of Robotic Systems*, 2003.

[46] J. J. L. Higdon, "The hydrodynamics of flagellar propulsion: helical waves," *Journal of Fluid Mechanics*, vol. 94, pp. 331–351, 1979.

[47] J. Avron, O. Kenneth, and D. Oaknin, "Pushmepullyou: an efficient micro-swimmer," *New Journal of Physics*, vol. 7, 2005.

[48] A. M. Leshansky, O. Kenneth, O. Gat, and J. E. Avron, "A frictionless microswimmer," *Proceedings of the National Academy of Sciences*, 2007.

[49] A. M. Leshansky and O. Kenneth, "Surface tank treading: Propulsion of Purcell's toroidal swimmer," *Physics of Fluids*, vol. 20, 2008.

[50] A. Filippov, "Drag and torque on clusters of n arbitrary spheres at low Reynolds number," *Journal of colloid and interface science*, vol. 229, no. 1, pp. 184–195, 2000.

[51] S. H. Lamb, *Hydrodynamics*, 6th ed. Dover Publications, 1945.

[52] A. M. Leshansky, "Actin-based propulsion of a micro-swimmer," *Physical Review E.*, vol. 74, no. 1, 2006.

[53] A. Najafi and R. Golestanian, "Simple swimmer at low Reynolds number: Three linked spheres," *Physical Review E*, vol. 69, p. 062901, 2004.

[54] F. Alouges, A. DeSimone, and A. Lefebvre, "Optimal strokes for low Reynolds number swimmers: An example," *Journal of Nonlinear Science*, vol. 18, pp. 277–302, 2007.

[55] D. Tam and A. E. Hosoi, "Optimal stroke patterns for Purcell's three-link swimmer," *Physical Review Letters*, vol. 98, February 2007.

[56] J. Avron, O. Gat, and O. Kenneth, "Optimal swimming at low Reynolds numbers," *Physical Review Letters*, vol. 93, no. 18, p. 186001, October 2004.

[57] S. Chattopadhyay, R. Moldovan, C. Yeung, and X. Wu, "Swimming efficiency of bacterium escherichia coli," *Proceedings of the National Academy of Sciences*, vol. 103, no. 37, pp. 13 712–13 717, September 2006.

[58] A. Shapere and F. Wilczek, "Geometry of self-propulsion at low Reynolds number," *J. Fluid Mech.*, vol. 198, pp. 557–585, 1989.

[59] ——, "Efficiencies of self-propulsion at low Reynolds number," *Journal of Fluid Mechanics*, vol. 198, pp. 587–589, 1989.

[60] H. A. Stone and A. D. T. Samuel, "Propulsion of microorganisms by surface distortions," *Physical Review Letters*, vol. 77, no. 19, pp. 4102–4104, November 1996.

[61] O. Reynolds, "On the motion of water," *Proceedings of the Royal Society of London*, vol. 35, pp. 84–99, 1883. [Online]. Available: http://www.jstor.org/stable/114354

[62] S. Kim and S. J. Karrila, *Microhydrodynamics: Principles and Selected Applications*, H. Brenner, Ed. Butterworth - Heinemann, 1991.

[63] H. Brenner, "The stokes resistance of an arbitrary particle," *Chemical Engineering Science*, vol. 18, pp. 1–25, Janurary 1963.

[64] R. B. Fuller, "Tensile-integrity structures," *U.S. Patent 3,063,521*, 1962.

[65] K. Snelson, "Continuous tension, discontinuous compression structures," *U.S. Patent 3,169,611*, 1965.

[66] R. E. Skelton, J. W. Helton, R. Adhikari, J.-P. Pinaud, and W. Chan, *The Mechanical Systems Design Handbook.* CRC Press, 2001, ch. An Introduction to the Mechanics of Tensegrity Structures.

[67] R. E. Skelton, J.-P. Pinaud, and D. L. Mingori, *The Mechanical Systems Design Handbook.* CRC Press, 2001, ch. The Dynamics of the Class 1 Shell Tensegrity Structure.

[68] R. E. Skelton, R. Adhikari, J.-P. Pinaud, and W. Chan, "An introduction to the mechanics of tensegrity structures," in *IEEE Conference on Decision and Control*, 2001.

[69] M. Masic, "Design, optimization, and control of tensegrity structures," Engineering Sciences (Aerospace Engineering), University of California, San Diego, July 2004.

[70] J.-P. Pinaud, M. Masic, and R. E. Skelton, "Path planning for the deployment of tensegrity structures," in *SPIE*, 2003.

[71] K. W. Moored and H. Bart-Smith, "The analysis of tensegrity structures for the design of a morphing wing," *Journal of Applied Mechanics*, vol. 74, pp. 668–677, July 2007.

[72] L. C. Chang and T. A. Read, "Plastic deformation and diffusionless phase changes in metals - the gold-cadmium beta phase," *Transactions AIME*, vol. 189, pp. 47–52, January 1951.

[73] G. K. White and S. B. Woods, "Conductivity of α-manganese," *Canadian Journal of Physics*, vol. 35, pp. 346–348, 1957.

[74] Z. Nishiyama and S. Kajiwara, "Electron microscope study of the crystal structure of the martensite in a copper-aluminium alloy," *Japanese Journal of Applied Physics*, vol. 2, no. 8, pp. 478–486, August 1963.

[75] F. E. Wang, W. J. Buehler, and S. J. Pickart, "Crystal structure and a unique "Martensitic" transition of tini," *Journal of Applied Physics*, vol. 36, no. 10, pp. 3232–3239, October 1965.

[76] F. E. Wang, B. F. DeSavage, and W. J. Buehler, "The irreversible critical range in the tini transition," *Journal of Applied Physics*, vol. 39, no. 5, April 1968.

[77] F. E. Wang and W. J. Buehler, "Additional unique property changes observed during tini transition," *Applied Physics Letters*, vol. 21, no. 3, pp. 105–106, August 1972.

[78] J. Aldrich, R. Skelton, and K. Kreutz-Delgado, "Control systhesis for a class of light and agile robotic tensegrity structures," in *American Control Conference*, June 2003.

[79] M. Artin, *Algebra*. Prentice Hall, 1991.

[80] W. M. Boothby, *An Introduction to Differentiable Manifolds and Riemannian Geometry*, 2nd ed. Academic Press, 2003.

[81] J. E. Colgate and K. M. Lynch, "Mechanics and control of swimming: A review," *IEEE Journal of Oceanic Engineering*, vol. 29, no. 3, pp. 660–673, July 2004.

[82] Y. Haga, Y. Tanahashi, and M. Esashi, "Small diameter active catheter using shape memory alloy," *Proc. Micro Electro Mech. Syst. Conf.*, pp. 419–424, January 1998.

[83] J. Happel and H. Brenner, *Low Reynolds Number Hydrodynamics.* Leyden: Noordhoff International Publishing, 1973.

[84] K. Hoffman and R. Kunze, *Linear Algebra*, 2nd ed. Prentice Hall, 1971.

[85] E. Kanso, J. Marsden, C. Rowley, and J. Melli-Huber, "Locomotion of articulated bodies in a perfect fluid," *Journal of Nonlinear Science*, vol. 15, pp. 255–289, 2005.

[86] J. M. Lee, *Introduction to Smooth Manifolds*, S. Axler, F. Gehring, and K. Ribet, Eds. Spring Science+Business Media, LLC, 2006.

[87] M. Mojarrad, "Auv biomimetic propulsion," *Oceans Conf. Rec.*, pp. 2141–2146, September 2000.

[88] N. Nakanishi and C. Wayman, "The effect of copper on the martensitic transformations in beta-phase aucd alloys," *Transactions of the Metallurgical Society of AIME*, vol. 227, pp. 500–504, April 1963.

[89] O. Raz and J. Avron, "Comment on "optimal stroke patterns for Purcell's three-link swimmer"," *Physical Review Letters*, vol. 100, January 2008.

[90] A. G. Rovira and J. M. M. Tur, "Control and simulation of a tensegrity-based mobile robot," *Robotics and Autonomous Systems*, 2008.

[91] Y. Sugiyama and S. Hirai, "Crawling and jumping by an deformable robot," *The International Journal of Robotics Research*, vol. 25, no. 5-6, pp. 603–620, May-June 2006.

[92] D. Tam and A. Hosoi, "Reply to comment on "optimal stroke patterns for Purcell's three-link swimmer"," *Physical Review Letters*, vol. 100, 2008.